View Article Online
View Journal

Nanoscale Horizons

The home for rapid reports of exceptional significance in nanoscience and nanotechnology

Accepted Manuscript

This article can be cited before page numbers have been issued, to do this please use: O. F. Odio, G. Tommasini, F. J. J. Teran, J. G. Ovejero, J. Rubín, M. Moros and S. Del Sol Fernandez, *Nanoscale Horiz.*, 2025, DOI: 10.1039/D5NH00254K.

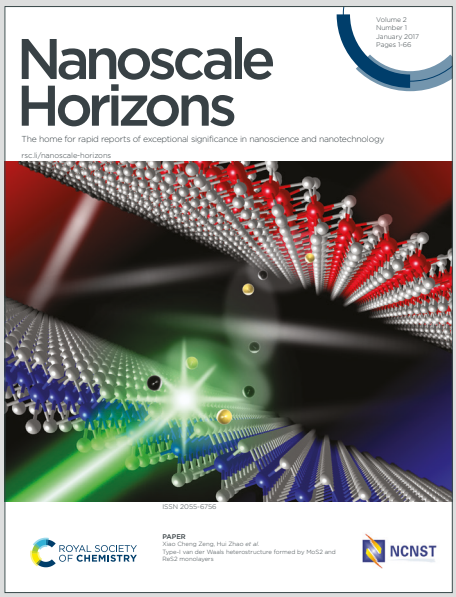

View Article Online
DOI: 10.1039/D5NH00254K

New concepts

We demonstrate a successful strategy to tune the heating efficiency of manganese ferrite nanoparticles ($Mn_xFe_{3-x}O_4$) by systematically varying the Mn^{2+} content, while maintaining consistent size and shape. This approach uncovers a direct correlation between Mn^{2+} content, effective anisotropy, and heating performance-key parameters for optimizing magnetic hyperthermia agents. A key discovery is that Mn^{2+} incorporation is not uniform-it begins at the nanoparticle surface, creating a compositional gradient. This gradient leads to superparamagnetic relaxation at the Mn-rich surface and ferrimagnetic behavior in the core. We identify an optimal Mn^{2+} content ($x \approx 0.60–0.70$) that maximizes effective anisotropy and specific loss power (SLP), while preserving biocompatibility (> 90% cell viability after 24 h). In contrast, high Mn^{2+} levels ($x \approx 1.40$) lead to structural defects, Mn^{3+} species, and reduced magnetization. Despite ion leaching during water transfer via PMAO coating, key magnetic properties are retained. This work provides critical new insight into how compositional control-independent of morphology and size-affects magnetic relaxation and heating performance, offering a rational framework for the design of stable, efficient, and safe magnetic nanoparticles in nanomedicine.

Unraveling the Mn^{2+} Substitution Effect on the Anisotropy Control and Magnetic Hyperthermia of $Mn_xFe_{3-x}O_4$ Nanoparticles

*Oscar F. Odio,[a] Giuseppina Tommasini,[b] F. J. Teran,[c,d] Jesus G. Ovejero,[e] Javier Rubín,[f] María Moros,[*b,g] and Susel Del Sol-Fernández[*b,h]*

[a]CONACyT-Instituto Politécnico Nacional, Centro de Investigación en Ciencia Aplicada y Tecnología Avanzada, 11500 Ciudad de México, México

[b]Instituto de Nanociencia y Materiales de Aragón, INMA (CSIC-Universidad de Zaragoza), C/ Pedro Cerbuna 12, 50009, Zaragoza, Spain.

[c]iMdea Nanociencia, Campus Universitario de Cantoblanco, 28049 Madrid, Spain

[d]Unidad de Nanomateriales Avanzados, iMdea Nanociencia, Unidad Asociada al CSIC.

[e]Instituto de Ciencia de Materiales de Madrid, ICMM (CSIC), Sor Juana Inés de la Cruz 3, 28049 Madrid, Spain.

[f]Dept. Materials Science and Metallurgy, Escuela de Ingeniería y Arquitectura (EINA), Universidad de Zaragoza, María de Luna 3, 50018 Zaragoza, Spain.

[g]Centro de Investigación Biomédica en Red de Bioingeniería, Biomateriales y Nanomedicina (CIBER-BBN), Spain.

[h] Present adress: Instituto de Ciencias Físicas, Universidad Nacional Autónoma de México, Av. Universidad s/n, Col. Chamilpa, Cuernavaca, Morelos 62210, México.

Corresponding authors: *Susel Del Sol-Fernández (sdelsol@icf.unam.mx) and María Moros (m.moros@csic.es)*

View Article Online
DOI: 10.1039/D5NH00254K

Abstract

Composition is a key parameter to effectively tune the magnetic anisotropy of magnetic nanoparticles, which in turn can modulate their structural-magnetic properties and final applications. The Mn^{2+} content of manganese ferrite nanoparticles ($Mn_xFe_{3-x}O_4$) deeply impact their structure, anisotropy, magnetism, and their heating capacity. However, a direct correlation between the Mn^{2+} content, magnetic properties and heating efficiency is not yet clear. Herein we report the synthesis of a wide range of $Mn_xFe_{3-x}O_4$ with x = 0.14 to 1.40, with similar polyhedral morphologies and sizes (13 to 15 nm). By varying the Mn^{2+} content (in the range of x = 0.0 up to 0.70), we successfully tuned the effective anisotropy while maintaining saturation magnetization nearly constant. Highest Mn^{2+} levels (x= 1.40) lead to structural changes and strain defects reflected in their poor saturation magnetization. Mn^{2+} substitution is not uniform, instead promotes a compositional gradient across the MNPs, with the surface layers having a higher concentration of Mn^{2+} than the core. The Mn^{2+}-rich surface likely exhibits superparamagnetic (SPM) relaxation, while the core remains predominantly ferrimagnetic (FiM). Water transference results in cations leaching, promoting vacancies and changes in the local ferrite structure but with minor impact on magnetic properties compared with initial MNPs. We obtained the optimal Mn^{2+} content that maximizes anisotropy for improved SLP values. Néel relaxation mechanism is warranted regarding variable composition when sizes and shapes are maintained. Our detailed analysis provides a better understanding of the effect of Mn^{2+} substitution on the heating efficiency through anisotropy modulation and straightforward guidance for the optimized MNPs design for magnetic hyperthermia.

Keywords: manganese ferrite nanoparticles, composition, anisotropy, soft ferrite, magnetism, magnetic hyperthermia

View Article Online
DOI: 10.1039/D5NH00254K

INTRODUCTION

Manganese ferrite nanoparticles ($Mn_xFe_{3-x}O_4$ MNPs) have attracted considerable attention for their potential applications in magnetic hyperthermia therapy (MHT) and magnetic resonance imaging (MRI)[1]. The substitution of Fe^{2+} by Mn^{2+} in the spinel structure can significantly alter their magnetic anisotropy, saturation magnetization (M_S), heating, and contrast efficiency due to the changes in their structural properties, including crystal structure, crystallite size, and lattice parameter[2,3,4]. While the impact of the Mn^{2+} content on the magnetic properties has been investigated in recent years using many different $Mn_xFe_{3-x}O_4$ MNPs[5–8], a direct correlation between the Mn^{2+} content and the magnetic properties is not yet clear. For instance, a broad range of $Mn_xFe_{3-x}O_4$ MNPs ($0 \leq x < 1$) prepared by the co-precipitation method showed a monotone increase of lattice parameters and heating capacity as the Mn^{2+} content increased, although these results could not be exclusively attributed to the Mn^{2+} content due to the size dispersion between samples[9]. Conversely, other authors did not find a correlation between Mn^{2+} content and magnetic properties of MNPs[7,10,11] or reported that the net M□ values did not consistently increase with Mn^{2+} content[12], even when a correlation between crystallite size and Mn^{2+} content was observed. Most notably, while computational modelling revealed a positive correlation between Mn^{2+} content and M_S[13], experimental data showed the opposite trend, which was attributed to a reduction in both the crystallite and magnetic diameters promoted by the incorporation of Mn^{2+}. Therefore, it is clear that one of the major challenges in studying how the composition of $Mn_xFe_{3-x}O_4$ MNPs impacts the structural-magnetic properties is maintaining similar average size, shape, and monodispersity across all samples, a fact that has been frequently overlooked.

These discrepancies across reports are also reflected in the optimal conditions for effective heat dissipation under an alternating magnetic field (AMF). For instance, similar Specific Loss Power (SLP) under an AMF have been observed in samples with markedly different compositions[14,15], whereas samples with similar compositions produced significant differences in terms of heat

View Article Online
DOI: 10.1039/D5NH00254K

generation depending on their internal structural defects[3]. The optimal Mn^{2+} content needed to efficiently dissipate heat under similar AMF conditions is yet not clear[4,16].

Therefore, further studies are necessary to better understand how composition can affect all these properties. More importantly, in many cases, these studies are performed exclusively in organic solvents, overlooking the impact that the water transference protocols can have on the final composition and the magnetic properties, potentially leading to partial or misleading interpretations. Soriano *et al*., reported Mn^{2+} leaching, and consequently, composition changes after water transference by using meso-2,3-dimercaptosuccinic acid (DMSA) and dopamine (DOPA) ligands [16]. This leaching could alter the crystal structure of the MNPs, significantly affecting their magnetic properties.

In this work, we present a detailed and systematic study of $Mn_xFe_{3-x}O_4$ MNPs ($x_{Empiric}$ = 0.14 - 1.40) with similar sizes and shapes, synthesized by a one-step thermal decomposition method, with the aim to correlate Mn^{2+} substitution effects in the structural, anisotropy, magnetic behaviour and heating properties of $Mn_xFe_{3-x}O_4$ MNPs. To achieve this, we synthesized seven MNPs samples by varying critical synthetic parameters, including the ratio of metallic precursors, final solvent volume, and the surfactant-to-metallic precursor ratio. A detailed investigation into the manganese oxidation state and allocation of cations across the samples revealed, for the first time, that the incorporation of manganese ions into the ferrite structure begins at the outermost layers and progressively extends toward the MNPs core. We concluded that Mn^{2+} substitution is not uniform; instead, a concentration gradient is observed, with a higher Mn^{2+} fraction at the surface. The Mn^{2+} rich surface dictated the preferential magnetic relaxation of the MNPs by Mössbauer spectroscopy. Finally, we investigated the impact of polymer coating on the final compositions of the $Mn_xFe_{3-x}O_4$ MNPs and crystal structure and magnetic properties. This work provides valuable insights into how tailoring the Mn^{2+} content can be used to effectively tune anisotropy and heating efficiency, thus advancing the understanding and optimization of MHT.

View Article Online
DOI: 10.1039/D5NH00254K

2. Materials and Methods

2.1. Materials

Iron(III) acetylacetonate ($Fe(acac)_3$, 97%), manganese(II) acetylacetonate ($Mn(acac)_2$, 98%), oleic acid (OA, 90%), 1,2-hexadecanediol (technical grade, 90%), dibenzyl ether (DBE, 90%), and poly(maleic anhydride-alt-1-octadecene) (PMAO) (MW = 30,000-50,000 Da), N-(3-dimethylaminopropyl)-N-ethylcarbodiimide hydrochloride (EDC) and 4-aminophenyl β-D-glucopyranoside, 3-(4,5-dimethylthiazol-2-yl)-2,5-diphenyltetrazolium (MTT), were purchased from Sigma-Aldrich. Tetramethylrhodamine 5-(and -6)-carboxamide cadaverine, (TAMRA) was purchased from Anaspec. All solvents were of analytical grade and used as received. Dulbecco Modified Eagle Medium (DMEM), fetal bovine serum (FBS), glutaMAX, antibiotic penicillin-streptomycin (10000 U/mL) were obtained from Gibco, 4′,6-diamidino-2-phenylindole dilactate (DAPI) and Prolong Diamond were obtained from Invitrogen. Phalloidin Alexa Fluor 488 were purchased from ThermoFisher Scientific. Glass 4-well chamber slide were obtained from Nunc™ Lab-Tek.

2.1.2 Synthesis of $Mn_xFe_{3-x}O_4$ MNPs

Different ratios of $Fe(acac)_3$/$Mn(acac)_2$ precursor (Fe/Mn ratio) were employed to tune the $Mn_xFe_{3-x}O_4$ composition from x = 0.14 to 1.4 through one-step thermal decomposition method[17]. The reagents amount used for all samples is shown in **Table S1 in the S.I**. Briefly, 15 mmol of the mixture of metallic precursors at different Fe/Mn ratios were dissolved in 150 mL of benzyl ether (BE) to obtain x = 0.14, 0.20, and 0.37 MNPs (large-scale synthesis, A Series), while 5 mmol of the metallic precursors, but maintaining the same Fe/Mn ratios were dissolved in 50 mL of BE to obtain the MNPs with x = 0.40, 0.70 and 1.4 (small-scale synthesis, B Series). For the small-scale synthesis, 10 mmol of 1,2-hexadecanediol (HDD) were used, whereas in large scale synthesis, 30 mmol were employed. The oleic acid (OA)/metallic precursors ratio was slightly increased from 2.6 (on large-scale) to 3 (on small scale). The temperature and heating rate at the nucleation and growth steps were maintained invariable in both syntheses. As common steps, the mixture was mechanically stirred (100 rpm) under

View Article Online
DOI: 10.1039/D5NH00254K

a smooth N_2 flow, heated to 200 °C for 2 hours (5 °C/min) and afterwards heated to 285 °C (3 °C/min) for another 2 hours. Finally, the mixture was cooled down to room temperature by removing the heat source. An ethanol excess was added to the mixture, the black material was precipitated and separated with a permanent magnet. The product was then resuspended in hexane, and precipitated with ethanol four times, resulting in a brownish-black hexane dispersion that was stored at 4 °C for future use.

2.1.3 Water transference

The transference into water was performed following a previously reported method with slight modifications[18]. In brief, 225 mg of poly(maleic anhydride-alt-1-octadecene) (PMAO) were added to a flask containing 195 mL of chloroform and placed in an ultrasonic bath for 30 min at room temperature. Subsequently, 10 mgFe/mL in 5 mL of $CHCl_3$ were added dropwise, and the mixture was sonicated for another 15 min. Afterwards, the solvent was slowly removed under vacuum (200 mbar, 40°C). The MNPs were then resuspended in 20 mL of NaOH 0.05 M and rota-evaporated (200 mbar, 70 °C) until complete evaporation of $CHCl_3$. At this point, the solution became clear as MNPs were completely transferred to water. MNPs were then filtered using 0.22 μm syringe filters. To remove the excess of unbound polymer, the MNPs suspension was centrifuged at 24000 rpm for 2 h four times and finally the MNPs were redispersed in milliQ water for further use.

2.1.4 Dye functionalization

To allow *in vitro* tracking, MNPs were labelled with a fluorescent dye (Tetramethylrhodamine 5-(and -6)-carboxamide cadaverine (TAMRA)[19]. To do so, 1% of the polymer monomers were modified with TAMRA (2 mg/mL) under magnetic stirring overnight in $CHCl_3$ before adding the MNPs.

2.1.5 Functionalization with glucose

Functionalization with glucose was performed by incubating 1 mg of Fe with 19 μmol of N-(3-dimethylaminopropyl)-N′-ethylcarbodiimide hydrochloride (EDC), 30 μmol of 4-aminophenyl β-D-glucopyranoside in 250 μl of SSB buffer pH 9 (50 mM of boric acid and 50 mM of sodium borate). After 3 h of incubation (600 rpm, 37 ºC), the ligand excess was removed by washing the MNPs with

View Article Online
DOI: 10.1039/D5NH00254K

phosphate-buffered saline (PBS 1X) pH 7.4 in a centrifugal filter with a membrane of 100 kDa molecular weight limit (Merck Millipore, Darmstadt, Germany) four times. Finally, the MNPs functionalized with glucose were filtered using syringe filters of 0.22 μm in sterile conditions and stored at 4 °C for further use.

2.1.6 Structural and colloidal characterization

The MNPs size, and morphology were evaluated by TEM using a Tecnai T20 (FEI, Netherlands) electron microscope working at an acceleration voltage of 200 kV. TEM samples were prepared by depositing 5 μL of dilute solution on a copper grid (200 mesh) and a posterior drying at ambient temperature prior to analysis. MNPs size distributions were obtained by measuring more than 200 MNPs with the Image J software. High resolution transmission electron microscopy (HRTEM), Scanning transmission electron microscopy (STEM), and energy-dispersive X-ray (EDX) images were obtained by a Tecnai F30 microscope with an accelerating voltage of 300 kV. Elemental mapping was performed using an Oxford EDS system in the drift corrector acquisition mode.

The crystal structure of the samples was identified by XRD powder patterns recorded using a Bruker D8 ADVANCE diffractometer working with CuK_α (λ = 1.5406 Å) radiation. The patterns were collected between 10° and 70° in 2θ range. Crystallite size and lattice strain determination were determined by the Scherrer formula as

$$\boldsymbol{d} = k\lambda/\beta \cos(\theta) \quad (\mathbf{1})$$

in which the anisotropy constants are k= 0.94, β is the full width at half maximum (FWHM), and θ is the Bragg angle in radians. Williamson and Hall method was used to obtain size and strain broadening by considering peak width as a function of 2θ as

$$\beta \cos\theta = \frac{\kappa\lambda}{D_{W-H}} + 4\varepsilon \sin\theta \quad (\mathbf{2})$$

where ε is the strain component crystal lattice, and $D_{W\text{-}H}$ is the average crystallite size obtained by the W–H analysis. By plotting βcosθ on y axis against 4sinθ on x axis, and their consequent linearly fitting,

View Article Online
DOI: 10.1039/D5NH00254K

we get the strain component from the slope (ε = slope) and the crystallite size from the intercept ($1 = K\lambda/D_{W-H}$)[20].

The elemental analysis was performed using an Inductively Coupled Plasma Optical Emission Spectrometry (ICP-OES) instrument (PerkinElmer mod. OPTIMA 2100 DV). Typically, 25 µL of a $Mn_xFe_{3-x}O_4$ MNPs suspension were digested in 1 mL of aqua regia in a volumetric flask at 60 °C overnight. Afterward, the flask was filled up with deionized water.

The surface chemistry was elucidated from FT-IR spectra using a PerkinElmer Spectrum Two spectrometer recorded in the range of 400 – 4000 cm^{-1}. Samples were lyophilized 24 hours before use.

Thermogravimetric analysis (TGA) of the metal precursors was performed in a PerkinElmer TGAQ5000 instrument from 40 to 500 °C at a rate of 10 °C/min and under a N_2 flow rate of 25 mL/min. Likewise, the MNPs organic contents were determined by TGA using a Universal V4.5A TA Instrument; the N_2 flow rate was 50 mL/min and the heating rate was set at 10 ºC/min until a final temperature of 800 ºC. MNPs in organic solvents were dried in air, while MNPs in water were lyophilized before measured.

The hydrodynamic diameters and zeta potential of the MNPs were measured using dynamic light scattering measurements (Malvern Zetasizer Nano) at room temperature. Samples were prepared at a concentration of 0.05 mg_{Fe}/mL in milli-Q water and sonicated 10 s before measurement.

X-ray photoelectron spectra were recorded with a Kratos AXIS Supra spectrometer equipped with a monochromatic source of Al Kα (1486.7 eV) working at 120 W with a base pressure of 10^{-9} Torr; the survey spectra were recorded at pass energy of 160 eV with a step size of 1000 meV, while the high resolution spectra were registered with a step size of 100 meV at pass energies of 20 and 40 eV for metal 2p and 3s regions, respectively. Due to the magnetic nature of the ferrite samples, the magnetic lenses were disabled, and it was operated under the Electrostatic-slot mode, setting an analysis area of *c.a.* 2 mm x 1 mm. The powdered samples were measured without any treatment, and the charge

View Article Online
DOI: 10.1039/D5NH00254K

neutralizer mode was kept on during the measurements. All spectra were analyzed with Thermo Avantage software package. The background was described with a Shirley-type equation. Relative atomic contents from the metal 2p region were computed from the Scofield sensitivity factors and the energy compensation factors given by the TPP-2M method. The high-resolution spectra in the metal 3s region were fitted with Voight profiles from a mixture of Gaussian and Lorentzian functions (80/20); details concerning the calculation of the relative atomic concentrations after the fitting procedure are provided in the Supporting Information.

Mössbauer spectra were collected using a constant acceleration spectrometer equipped with a 5 mCi Co57/Rh source. The velocity scale was calibrated with a-Fe foil and analysed using the MossWinn 4.0 software. Isomer shift values are given with respect to α-Fe.

2.2 Determination of iron concentration

The determination of iron concentration was performed following a previously reported protocol[21] and to adjust iron concentration before glucose functionalization. In brief, 5 µl of MNPs was diluted in 45 µl of solvent (hexane or water) and digested with 100 µl of aqua regia solution (3:1 HCl:HNO_3) at 60 °C for 15 min. Then, the samples were diluted up to 300 µl with miliQ water. At this point, 50 µl (in triplicate) was used for the iron quantification by mixing the digested samples with 60 µl of 0.25 M 1,2-dihydroxybenzene-3,5-disulfonic acid (Tiron). This molecule forms a coloured complex with iron, and it can be measured by spectrophotometry at λ = 480 nm using a microplate spectrophotometer (BioTek Synergy H1 UV/VIS, Agilent Technologies, Santa Clara, CA, USA) and compared with a standard calibration curve obtained with solutions of known iron concentrations (0-1000 µg Fe/mL). This protocol was performed after each glucose functionalization.

2.3 Conventional calorimetry measurement

The determination of magnetic losses from MNP suspensions was performed by non-adiabatic calorimetry measurements using a nanoScale Biomagnetics D5 series device as AC magnetic field

View Article Online
DOI: 10.1039/D5NH00254K

generator. The equipment is composed of a generator with a frequency ranging from 100 - 763 kHz and a magnetic coil (magnetic field range: 0 - 60 mT). The suspension (1 mL) was placed into a glass vial located at the center of the magnetic induction coil inside an isolating holder. The temperature was measured with an optic fiber sensor Neoptix T1 incorporated into the equipment (measurement range - 40 to 200 °C) for 300 s. Thermal measurements of MNPs in water were performed at 2 mg_{Fe+Mn}/mL and 1 mg_{Fe+Mn}/mL for low (155 kHz) and high (763 kHz) frequency, respectively. Different magnetic field intensity was used depending on the selected frequency: f = 763 kHz, H = 3.8, 8.0, 16.8, 28.8 kA/m and for f = 155 kHz, H = 16.8, 28.8 and 44.6 kA/m. The effect of viscosity (1 mL of 0%, 2% and 50% of glycerol in double distilled water) was evaluated for selected samples at f = 763 kHz. The temperature change was measured as a function of time (dT/dt), and the initial linear slope (t = 30 s) was used to evaluate the heating efficiency in terms of SLP. The SLP values were calculated according to the following expression:

$$SLP = \frac{dT}{dt}\frac{Cdmd}{m_{Fe+Mn}} \quad (3)$$

where the Cd is the mass specific heat of the dispersion media, md is the mass dispersion, m_{Fe+Mn} is the iron and manganese masses related to the MNP diluted in the dispersion and dT/dt|max is the maximal temperature slope immediately after switching H_{AC} on. Solvents in our experiment were water (Cd_{water}= 4.18 J/g.°C) or water with different glycerol fractions from 0 to 50%, considering $Cd_{glycerol}$ = 2.43 J/g.°C and for mixed water-glycerol Cdmix= 3.30 J/g.°C. Sample volume employed for the experiment was 1 mL.

2.4 Magnetic measurement

Static conditions: magnetic characterization of MNPs under static conditions were carried out in a superconducting quantum interference device (SQUID, Quantum Design) magnetometer at distinct temperatures from 5 K up to 300 K fields up to 4000 kA/m. The studied magnetic suspensions were lyophilized to get a powder, which was put into a gelatin capsule (~ 5 mg per sample), and immobilized

View Article Online
DOI: 10.1039/D5NH00254K

with cotton wool. Magnetization units were normalized to the organic content measured by TGA. Saturation magnetization (M_S) values were calculated by extrapolating to infinite field the experimental results obtained in the high field range where the magnetization linearly increases with 1/H.

Dynamical conditions: AC magnetometry measurements of the studied magnetic suspensions (m_{Fe+Mn} = 5 mg) were carried out by commercial inductive magnetometers (Advance AC Hyster Series; Nanotech Solutions, Spain) at 150 kHz and 300 kHz and field intensities up to 24 kA/m. Each magnetization cycle is obtained out of three repetitions, resulting in the averaged magnetization cycle, related magnetic parameters (H_C, M_R, Area) and magnetic losses. SAR values were determined for the expression[22].

$$SAR = Af \quad (4)$$

where A is the AC magnetic area and f is AC magnetic field frequency. Magnetization units were normalised by the magnetic mass (i.e. iron plus manganese masses).

2.5. Biological assays

2.5.1 Cell culture

MIA PaCa-2 human and male pancreatic adenocarcinoma cells (ATCC® number CRL-1420) were cultured in Dulbecco's modified Eagle's medium (DMEM) supplemented with 10% fetal bovine serum, 5% L-glutamine, and 5% penicillin/streptomycin antibiotics and maintained in a humidifier incubator at 37 °C in a 5% CO_2 atmosphere.

2.5.2 *In vitro* cytotoxicity assay

MTT assay was performed to evaluate cell viability of MNPs treated cells. MIA PaCa-2 cells were seeded in 96-well plates and cultured for 24 h (5×10^3 cells/well). MNPs functionalized with glucose at various concentrations (25, 50, 100, and 150 µg Fe/mL) were added in DMEM and incubated for 24 h at 37 °C. Cells were thoroughly washed with PBS, and 10 µl of MTT solution (5 mg/mL in PBS) in a final volume of 100 µL (DMEM w/o phenol red) was added to each well. Following 30 min of

View Article Online
DOI: 10.1039/D5NH00254K

incubation at 37 °C, the plates were centrifugated at 1250 rpm for 30 minutes and formazan salts were dissolved with 100 µl of DMSO in agitation for 15 min at 37 ºC; the resulting absorbance was determined at λ = 540 nm on a microplate reader (BioTek Synergy H1 Multimode Microplate Reader). Control cells without MNPs (negative control) were also analysed**.** Data are expressed as the percentage of cell viability normalized for the control condition and are the results of three independent biological replicates.

2.5.3 Internalization by fluorescence microscopy

MNPs internalization was studied by fluorescence microscopy (using MNPs modified with TAMRA fluorophore) and ICP-OES. *Fluorescence microscopy*. To perform fluorescence microscopy analysis, 5×10^4 cells were seeded on a glass 4-well chamber slide. After 24 h of culturing, cells were treated with 100 µg Fe/mL of MNPs functionalized with glucose and incubated at 37ºC (5% CO_2) for 24 h. Noninternalized MNPs were removed by washing with PBS thrice. Cells were fixed with 4% of paraformaldehyde for 15 min at room temperature and washed twice with cold PBS. After that, F-actin staining was performed using phalloidin AlexaFluor 488 following manufacturer instructions. For nuclei labelling cell were incubated 10 min at RT with 0,6 µM of DAPI. Finally, the slide was mounted using freshly prepared ProLong reactive. Fluorescence microscopy images were performed using an inverted microscope (Nikon Eclipse Ti-E, Amsterdam, The Netherlands).

Statistical Analysis

All data are presented as mean ± standard deviation (SD). One-way analysis of variance (ANOVA) and Tukey test were applied to calculate the differences between the values. Values of $p < 0.05$ were considered statistically significant.

3. RESULTS AND DISCUSSION

View Article Online
DOI: 10.1039/D5NH00254K

3.1 Design of a library of $Mn_xFe_{3-x}O_4$ MNPs. Structural changes as results of manganese substitution.

Several $Mn_xFe_{3-x}O_4$ MNPs with different Mn^{2+} content but similar sizes and shapes were synthesized by a one-step thermal decomposition method, modifying different parameters such as the metallic precursors ratio ($Fe(acac)_3/Mn(acac)_2$), the surfactant/precursors ratio (OA/metallic precursors) and/or the final solvent volume (see **Table S1 in the S.I.**). In all cases, the remaining synthetic parameters, that is, the heating rate, reaction time, and the temperatures during the nucleation and growth steps, were maintained constant. Benzyl ether (BzE) was selected as a passive solvent due to its lack of hydroxyl groups capable of iron chelation, thereby minimizing a direct influence on the MNPs' size and shape[23].

To elucidate the influence of the surfactant concentration on the overall composition, two $Mn_xFe_{3-x}O_4$ MNPs were synthesized using the same $Fe(acac)_3/Mn(acac)_2$ ratio (6.5) and final solvent volume (50 mL) while slightly varying the OA/metallic precursors ratio from 2.6 to 3 (see **Table S2 in the S.I.**). The empirical x value, determined by ICP-OES, remained unchanged for both samples ($x_{Empiric} = 0.18$), indicating that under these synthetic conditions Mn^{2+} incorporation was insensitive to slight variations in the amount of surfactant. However, the sample synthesized with the lower OA/metallic precursors ratio exhibited more irregular shapes (**Figure S1 in the S.I**.). A plausible explanation is that limited OA availability leads to a preferential growth of the initial seeds along certain crystal directions (particularly those normal to the facets ({111} and {110}), which are poorly stabilized by the OA, resulting in more irregular shapes. In contrast, sufficient OA during the nanocrystal growth ensures well-capped and stabilized crystal facets, leading to MNPs with controlled faceted shapes[24,25].

The overall composition of the MNPs was then varied by changing the metallic precursor ratio and final solvent volume. Two series of $Mn_xFe_{3-x}O_4$ MNPs were synthesized: **A Series (large-scale synthesis)**, where the MNPs were prepared in 150 mL of BzE, and **B Series (small-scale synthesis)**

View Article Online
DOI: 10.1039/D5NH00254K

obtained using 50 mL of BzE. Mn^{2+} content in both series was adjusted by changing the initial $Fe(acac)_3/Mn(acac)_2$ ratios, corresponding to theoretical *x* values of 0.40, 0.75, and 1.0 (**Table 1 in the S.I.**). In all cases, the Mn^{2+} incorporated into the final MNP was much lower than the theoretical values, based on the amount of Mn^{2+} added as initial precursors. This effect has already been described and is likely due to various factors, such as differences in the decomposition temperatures of the two precursors (most of the $Mn(acac)_2$ decomposes 60 °C higher than $Fe(acac)_3$, see **Figure S6** left panel **in the SI**) and/or the ionic radii differences between Mn^{2+} and Fe^{2+} [16,26]. However, this effect was not observed in other studies when using the same metallic precursors[13,3] or oleates[2]. Nevertheless, in the latter, octadecene was used as the synthetic solvent instead of BzE, making a direct comparison difficult. Moreover, it is noted that in both series of MNP samples (A and B), the higher the molar concentration of the Mn^{2+} precursor used in the synthesis, the higher the Mn content in the final ferrite stoichiometry **(Table 1)**. This tendency, determined by ICP-OES, was further confirmed by EDX for samples belonging to A Series (**Figure S2 in the S.I.**).

Additionally, the solvent volume influenced the incorporation of Mn^{2+} into the spinel structure (**Figure S3 in the S.I.**). When the same $Fe(acac)_3/Mn(acac)_2$ ratio was used, the amount of Mn^{2+} incorporated into the spinel structure was consistently higher in the B Series (smaller volume of solvent) than in A Series (larger solvent volume) **(Table 1)**. One hypothesis is that the use of a smaller solvent volume facilitates higher and more uniform temperatures throughout the mixture, improving the decomposition of $Mn(acac)_2$ precursor and thereby reducing the critical gap between the decomposition of metallic precursors and the saturation limit for particle nucleation[27]. To further increase the Mn^{2+} content in the final MNPs, an additional synthesis was performed only for **Serie B,** as was the one incorporating more Mn^{2+} in the final structure (x_{Theo} = 1.5, $Mn_{1.50}Fe_{1.50}O_4$). The empirical *x* value was similar to the theoretical one ($x_{Empiric}$ = 1.40, $Mn_{1.40}Fe_{1.60}O_4$).

View Article Online
DOI: 10.1039/D5NH00254K

Table 1. Summary of $Fe(acac)_3/Mn(acac)_2$ molar ratio employed in the synthesis and theoretical (x_{Theo}) and empirical ($x_{Empiric}$) stoichiometry of the $Mn_xFe_{3-x}O_4$ ferrites. The average sizes were determined by TEM (D_{TEM}). Peak position at 311 reflection and crystallite sizes determined by XRD using Sherrer equation (D_{XRD}) or Williamson-Hall method (D_{W-H}).

Samples	Fe/Mn precursors' molar ratio in synthesis	x_{Theo} value	$x_{Empiric}$ value	Measured Formula	D_{TEM} (nm)±SD	(311) peak pos. (2θ°)	D_{XRD}[a] (nm)±SD	D_{W-H}[b] (nm)±SD
A Series (150 mL)	6.5	0.40	0.14	$Mn_{0.14}Fe_{2.86}O_4$	14 ± 3	35.43	12 ± 1	12 ± 1
	3	0.75	0.23	$Mn_{0.23}Fe_{2.77}O_4$	13 ± 3	35.40	13 ± 1	18 ± 2
	2	1.0	0.37	$Mn_{0.37}Fe_{2.63}O_4$	15 ± 2	35.39	14 ± 2	15 ± 1
B Series (50 mL)	6.5	0.40	0.18	$Mn_{0.18}Fe_{2.82}O_4$	13 ± 2	35.42	14 ± 1	15 ± 1
	3	0.75	0.47	$Mn_{0.47}Fe_{2.53}O_4$	15 ± 1	35.39	13 ± 1	16 ± 2
	2	1.0	0.70	$Mn_{0.70}Fe_{2.30}O_4$	14 ± 2	35.35	13 ± 1	16 ± 1
	1	1.5	1.40	$Mn_{1.40}Fe_{1.60}O_4$	14 ± 1	35.26	13 ± 1	15 ± 2

a) Calculated by Scherrer method.
b) Calculated by Williamson-Hall method.

As shown in **Figure 1A and Table 1**, all the synthesis yielded MNPs with similar polyhedral morphologies and sizes ranging from 13 to 15 nm, regardless of the metallic precursor's ratio or the solvent volume used. These results are in good agreement with previous works using the same precursors but different synthetic methods[13,16,28]. Controlling particle size and shape is crucial to isolate and accurately assess the influence of composition on the anisotropy and magnetic heating, while minimizing the influence of these parameters.

To investigate whether the tuned compositions could result in a single or core/shell MNP structure as previously reported,[29,30] we used STEM-Energy-Dispersive X-ray Spectroscopy on selected $Mn_xFe_{3-x}O_4$ MNPs with the lowest, medium, and highest Mn^{2+} content ($x_{Empiric}$ = 0.14, 0.70 and 1.40 respectively) (**Figure 1B**). The chemical maps showed that the Mn and Fe signals were present along the magnetic cores and the absence of a marked core-shell structure and, thus, the successful synthesis of a unique $Mn_xFe_{3-x}O_4$ core in agreement with several reports[16,3,2].

View Article Online
DOI: 10.1039/D5NH00254K

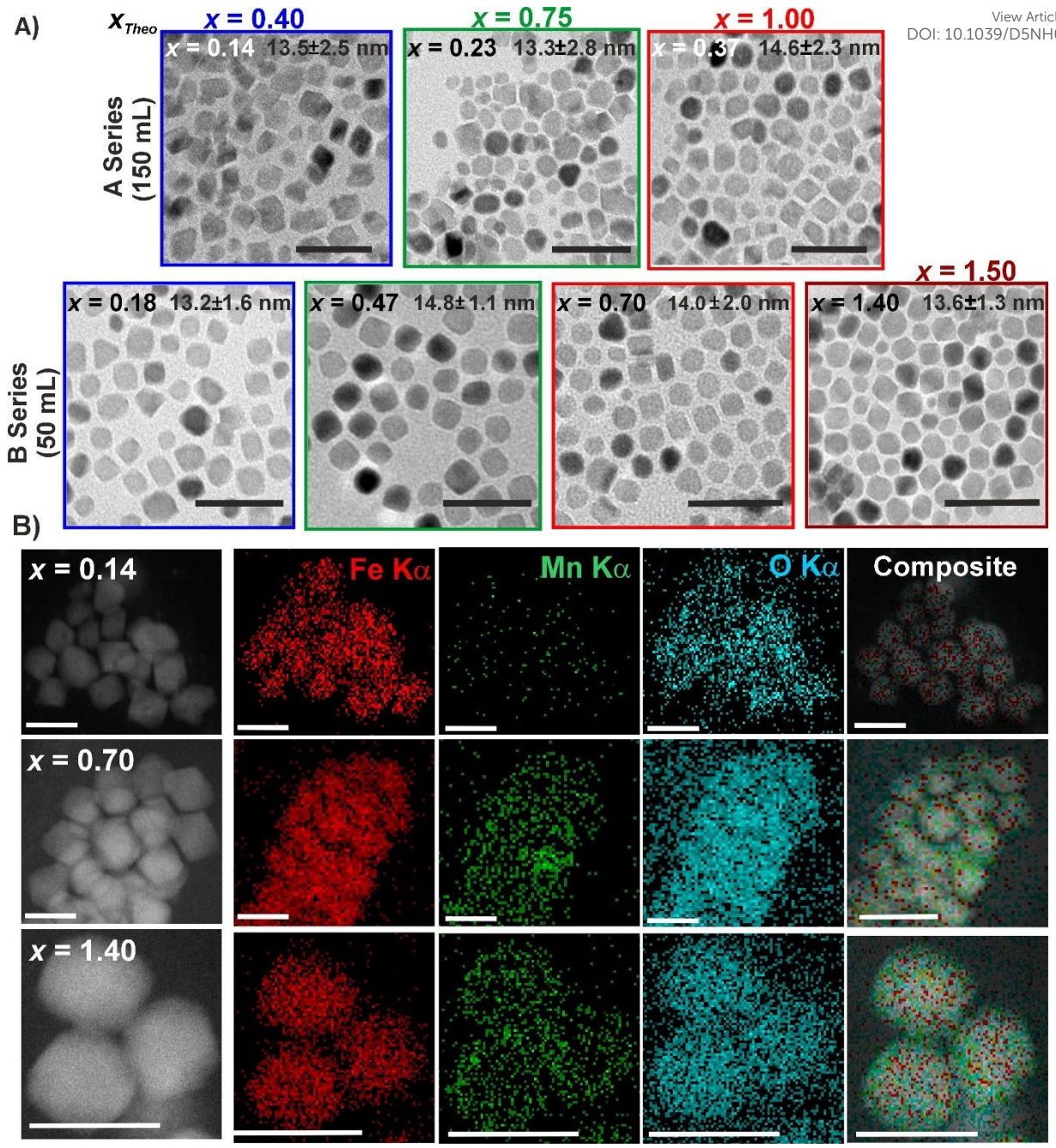

Figure 1. A) TEM images of $Mn_xFe_{3-x}O_4$ MNPs with varying Mn^{2+} content ($x_{Empiric}$ = 0.14 to 1.40). The samples with initial Fe/Mn precursor amount of x_{Theo} = 0.40, 0.75, 1.0, and 1.50 are highlighted with blue, green, red, and brown boxes, respectively. Inset: empirical x value for each sample determined by ICP-OES along with their respective size diameters. Scale bar: 50 nm. **B)** STEM-EDX mapping images of $Mn_xFe_{3-x}O_4$ MNPs with the lowest, medium, and highest content of Mn^{2+} ($x_{Empiric}$ = 0.14, 0.70, 1.40). Scale bar: 50 nm ($x_{Empiric}$ = 0.14 and 0.70), 20 nm ($x_{Empiric}$ = 1.40).

For further analysis, we selected samples with increasing Mn^{2+} content, that is, $x_{empiric}$ = 0.14, 0.23, 0.37, 0.47, 0.70, and 1.40. **Figure 2A** shows the evolution of the XRD patterns of these MNPs together with the positions of the peaks corresponding to the $MnFe_2O_4$ spinel-type phase (PDF file 96-230-

View Article Online
DOI: 10.1039/D5NH00254K

0619 in the ICDD powder diffraction file database). Interestingly, the presence of additional reflections (denoted with an asterisk) corresponding to the $Fe_{1-x}O$ phase (PDF file 96-101-1199) appeared in the samples with Mn^{2+} content $x \geq 0.70$. The coexistence of both magnetic phases can have a high impact on the structural, magnetic, and heating properties of ferrite MNPs, as previously reported[3,31,32]. As expected, we found a gradual shift toward lower angles while increasing the Mn^{2+} content from 35.43 ($x_{Empiric}$ = 0.14) to 35.26 ($x_{Empiric}$ = 1.40), taking as reference the reflection (311). This corresponds to an increase in the cubic unit cell parameter due to the substitution of smaller host ions (0.65 Å for Fe^{3+} and 0.78 Å for Fe^{2+}) by a larger Mn^{2+} (0.83 Å)[33], to the appearance of strains inside the spinel structure[2,20]. To further confirm this hypothesis, we calculated the strain (ε) component inside the spinel structure following the Williamson-Hall (W-H) method[33] by XRD patterns and measured the lattice distance for selected samples by HRTEM[33]. As shown in the HRTEM images (**Figure 2B)**, the inverse FFT of the (220) plane distance increased from 0.286 nm ($x_{Empiric}$ = 0.23) to 0.290 nm ($x_{Empiric}$ = 0.37), in agreement with the XRD patterns. On the other hand, from the fitting of the W-H plot, we found that when Mn^{2+} content increased from $x_{Empiric}$ = 0.14 up to 1.40, the lattice strain increased from 0.20 x 10^{-3} to 2.12 x 10^{-3} (**Table S3 in the S.I.**), indicating a larger lattice spacing due to the introduction of Mn^{2+}. This ultimately leads to the appearance of uniform tensile strain[20], which corresponds to the left shift shown in the XRD patterns (**Figure 2A**). Although the lattice defects varied among the samples, the effect was more prominent for the sample with the highest content of Mn^{2+} ($Mn_{1.40}Fe_{1.60}O_4$).

The average crystallite sizes calculated using Scherrer's formula (D_{XRD}) and the W-H method (D_{W-H}) ranged from 12 nm to 14 nm and from 12 nm to 18 nm, respectively (**Table 1**). In all cases, the mean MNP diameters obtained from TEM (D_{TEM}) matched relatively well with the crystal sizes determined by XRD using both methods, indicating a single-crystal structure. No clear correlation between the Mn^{2+} content and the crystallite size was observed. Similar findings have been reported for $Mn_xFe_{3-x}O_4$ nanoparticles with homogeneous characteristics (~6 nm in size, uniform shape, and oleic acid

View Article Online
DOI: 10.1039/D5NH00254K

coating) in the range of x= 0.11 to 0.49 [12]. On the contrary, other works have reported an increase of the crystallite size for $Mn_xFe_{3-x}O_4$ MNPs obtained by a similar synthetic procedure but using 1-octadecene as a solvent, or by co-precipitation in water using metallic chloride precursors.[4,13] In contrast, a decrease in the crystallite size from 16.7 nm (x = 0) to 10.2 nm (x = 1) has been observed for Mn-doped $CoFe_2O_4$ ferrites[34]. These discrepancies may be attributed to structural defects frequently associated with the increase of Mn^{2+} in the spinel structure, which could cause contraction of the crystal structure. In our case, the use of BzE as the solvent, rather than more reducing solvents like 1-octadecene, likely helped minimize the formation of such defects[3]. Therefore, even when an increase in the Mn^{2+} content may have introduced some strain defects, these were insufficient to impact the final crystallite size of our MNPs.

3.2 Manganese substitution induces changes in oxidation state, relocation of cations, and sample heterogeneity.

To shed light on the oxidation state of the cations in the samples under study, we analyzed the photoelectron spectral region corresponding to the Mn 3s and Fe 3s region using x-ray photoelectron spectroscopy (XPS). The fitting results for the $Mn_xFe_{3-x}O_4$ MNPs with $x_{Empiric=}$ 0.23, 0.37, 0.47, 0.70, and 1.40 are shown in **Figure S5** and summarized in **Table S4** of the S.I; also, a detailed explanation of the spectral features found in this region is provided in **Section 1** of the S.I.

All spectra were successfully fitted with two sets of doublets and a minor contribution at higher binding energy (BE). The doublet with the lower BE (80-90 eV) corresponds to Mn cations, and the one with higher BE (90-100 eV) is attributed to Fe cations. The occurrence of these doublets is primarily due to the multiplet splitting of the ionic final-state configuration $3s^13d^n$, arising from the exchange interactions between the remaining 3s core-electron and the unpaired electrons in the valence 3d shell of the transition metals[35–37]. This interaction gives rise to a high spin (lower BE) and a low spin (higher BE) final-state configurations, where the electron spins in the 3s and 3d shells are coupled either parallel or anti-parallel, respectively. Since the magnitude of the resulting energy splitting (ΔBE) is proportional to the total spin density of the 3d shell, this value has been used to identify the oxidation

View Article Online
DOI: 10.1039/D5NH00254K

state of the ion[38,39], especially for compounds with high degree of ionicity. In addition, as the ΔBE is also proportional to the exchange integral between the 3s and 3d shells, it could be sensitive to covalent and ligand field effects[40,41].

View Article Online
DOI: 10.1039/D5NH00254K

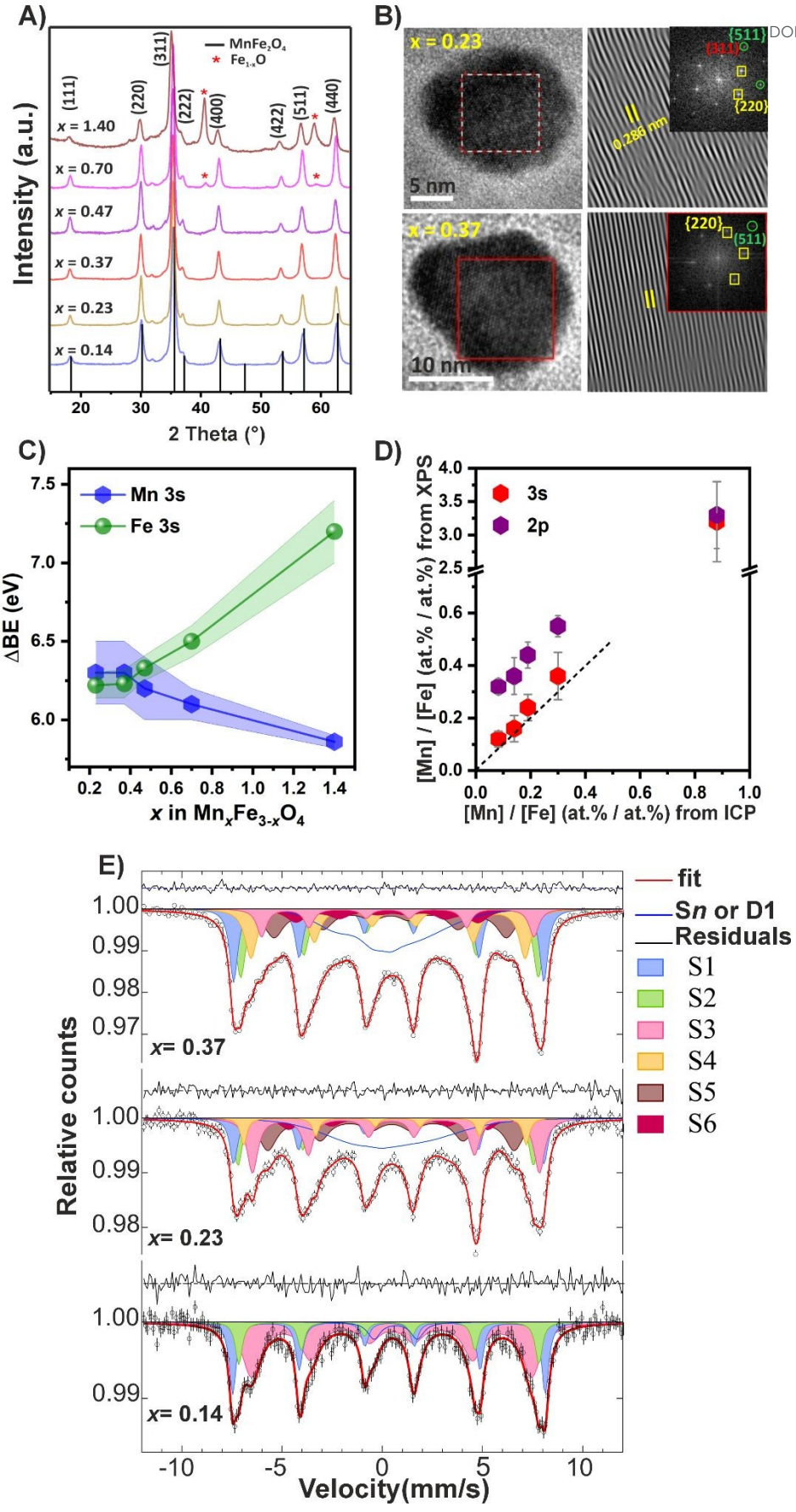

View Article Online
DOI: 10.1039/D5NH00254K

Figure 2. A) Evolution of the XRD pattern of the full set of $Mn_xFe_{3-x}O_4$ MNPs with $x = 0.14$ up to 1.40 with the corresponding Bragg positions of $MnFe_2O_4$ reference (black lines) and Fe_xO (red asterisk) **B)** HRTEM images of samples with $x_{Empiric} = 0.23$ and 0.37 and its FFT and inverse FFT of the plane (220). **C)** Energy splitting of the Mn 3s and Fe 3s doublets as function of the ferrite stoichiometry computed from XPS. **D)** Mn/Fe atomic ratios computed from the 2p and 3s XPS signals vs the compositional data obtained from ICP, for the samples with ferrite stoichiometry of $x_{Empiric} = 0.23$, 0.37, 0.47 and 1.40. **E)** Mössbauer spectra of $x_{Empiric} = 0.14$, 0.23 and 0.37 MNPs

Figure 2C shows the behavior of the computed ΔBE values after spectral fitting. Remarkably, it is apparent a close correlation between the energy splittings of both Mn 3s and Fe 3s doublets. For the samples with $x_{Empiric} \leq 0.37$, the splitting of the Mn 3s doublet is higher than 6.2 eV, which strongly suggests that the manganese ions are preferentially in the divalent state, with no evidence of oxidized species[39,42]. These values are consistent with the results reported elsewhere for several manganese ferrites[43,44]. At these low Mn^{2+} levels ($x_{Empiric} \leq 0.37$), the recorded values of ΔBE for the Fe 3s doublet around 6.2-6.3 eV suggest the coexistence of Fe^{2+} and Fe^{3+} cations due to the partial substitution of Mn^{2+} in the ferrite structure[36,37,40,41]. It is worth to note that, as the Mn^{2+} content in the ferrites increases (e.g., in samples with $x_{Empiric} = 0.47$ and 0.70), a gradual decrease in ΔBE of Mn 3s doublet is observed. Such behavior could be related with either the appearance of small fraction of Mn in a higher oxidation state ($x_{Empiric} \geq 0.70$) or a less ionic environment of the Mn^{2+} ions in the spinel structure[45,46], which could suggest: *i)* a gradual occupancy of tetrahedral sites by Mn^{2+} or *ii)* a higher probability of $–Mn^{2+}–O–Mn^{2+}–$ sequences at the expense of $–Mn^{2+}–O–Fe^{3+}–$ sequences. At the same time, the splitting of the Fe 3s doublet increases, which is consistent with the progressive substitution of Fe^{2+} cations by Mn^{2+} in the spinel structure. In the case of the sample with the highest Mn^{2+} content ($x_{Empiric} = 1.40$), the further reduction of the Mn 3s ΔBE to 5.9 eV may indicate the coexistence of a Mn^{3+} fraction forming oxidized species. Meanwhile, the high value for the Fe 3s ΔBE (7.2 eV) indicates the predominant presence of Fe^{3+} cations inside the oxygen lattice consistent with a highly ionic environment[36,40,41,47]. This observation suggests a preferential occupancy of the octahedral sites (B) by Fe^{3+}[45,46]. Additionally, the likely absence of Fe^{2+} ions is consistent with a massive substitution of Mn in the ferrite structure.

View Article Online
DOI: 10.1039/D5NH00254K

The recorded XPS spectra also provided a conclusive clue on the heterogeneity of the samples by analyzing the 2p and 3s signals of the cations. We have computed the Mn/Fe atomic ratios from the spectral fittings of the 3s region (**Section 1 in the SI**) and the direct integration of the corresponding 2p high-resolution spectra (see **Figure S4 in the SI**). Using the TPP-2 formula previously reported[48], it is possible to estimate the inelastic mean free path (IMFP) of the photoelectrons coming from both spectral regions, which is a function of the photoelectron kinetic energy. For the Mn and Fe 3s photoelectrons with kinetic energy around 1400 eV, the IMFP is roughly 2.1 nm; in the case of the Mn and Fe 2p photoelectrons with kinetic energy about 800 eV, the IMFP is roughly 1.4 nm. Therefore, the information depth (3 times the IMFP) derived from the 2p and 3s signals covers the outermost 4 nm (2p) and the topmost 6 nm (3s) of the ferrite MNP, respectively. The comparison between the computed Mn/Fe atomic ratios is displayed graphically in **Figure 2D**, where both data sets derived from XPS are plotted against the Mn/Fe ratios obtained by ICP quantification. The dashed line with unitary slope represents the ideal case where the surface composition computed by XPS agrees with the overall composition of the MNP (ICP). From the graph, it is apparent that for the samples with $x_{Empiric} \leq 1.40$, the estimated cation composition along the outermost 6 nm of the MNP (3s) is like the composition from the ICP data, which is consistent with the estimated average MNP diameters of 13-15 nm from TEM and DRX measurements. The fact that the 3s data is slightly biased toward higher Mn content in all samples, could suggest that the Mn ions entering the ferrite structure do not reach the very core of the MNP. On the other hand, by comparing the data sets from the 2p and 3s signals, it is noticeable that for $x_{Empiric} \leq 1.40$ the Mn/Fe atomic ratio is systematically higher in the first 4 nm than if it is computed extending the probed depth for other 2 nm inside the MNP core. In other words, the nanoparticle's surface is enriched in Mn^{2+} content with respect to the deeper zones near the core. This fact could indicate that the incorporation of Mn into the ferrite structure starts in the most superficial layers and then extends toward the interior of the MNP.

View Article Online
DOI: 10.1039/D5NH00254K

Previous works[50–52] on doped ferrites have also reported this surface enrichment of the doping element, which seems to be related with differing onsets of the nucleation process: when the nucleation step of the doping-containing monomers occurs late compared to the nucleation of the matrix-containing monomers, the doping element is initially out of the core of the resulting particle, and can develop a gradient concentration as function of its diffusivity across the particle. This phenomenon is triggered by the aforementioned 60°C difference in the decomposition temperature between Mn^{2+} and Fe^{2+} acetylacetonates, which produces monomers at different stages of the reactions that nucleate inhomogeneously. A thorough understanding of the magnitude of the Mn gradient along the nanoparticle structure as a function of ferrite stoichiometry requires more in-depth studies using STEM-EELS and XPS combined with Ar ion cluster sputtering, which will be the subject of future work.

3.3 Mn substitution and heterogeneity in Mn content along the MNP dictates the predominant magnetic relaxation regime.

To elucidate the impact of the compositional heterogeneity and Mn substitution on the magnetic behaviour, we recorded Mössbauer spectra at room temperature. **Figure 2E** shows the corresponding spectra for samples with $x_{Empiric}$ = 0.14, 0.23 and 0.37. The general aspect of the spectra is different from that of bulk $Mn_xFe_{3-x}O_4$[49] and similar to that of nanostructured ferrite MNPs[50]. At first sight, it is apparent that the samples display magnetic order, owing to the hyperfine peaks that dominate the profiles; in addition, the occurrence of a broad central background, especially for the samples with higher Mn^{2+} content, could indicate the presence of partially superparamagnetic (SPM) components[50]. The simultaneous presence of both features shows that the MNPs cannot be simply described as homogeneous with a constant Mn^{2+} concentration, and thus the same magnetic behaviour throughout the particle or in all the particles. Therefore, we tried an analysis intending to separate the ferrimagnetic (FiM) behaviour from the SPM-like one by considering: **1)** sextets with hyperfine fields (HF) above a threshold value of 40 T (FiM portion contribution)[50–52], and **2)** sextets with lower HF values and poorly structured central contributions (fraction with SPM-like behaviour). These last features could include

View Article Online
DOI: 10.1039/D5NH00254K

either a broad singlet, or a quadrupolar doublet, or a Voigt-based Gaussian distribution of HFs and isomer shifts (IS)[53]; this type of distribution can provide flexibility to the fits to simulate more complex structures at the centre of the spectrum.

The results of the fits are shown in **Figure 2E** and summarized in **Table S10** of the S.I. For the sample with $x_{Empiric}$ = 0.14, the spectrum was successfully fitted with three hyperfine sextets and a small quadrupolar doublet. The two sextets with higher HFs and IS values around 0.3 mm/s are attributed to Fe^{3+} ions; the one displaying the largest HF (**S1**) corresponds to the cations that occupy A sites, while the other sextet (**S2**) is assigned to the cations occupying the B sites. The third sextet (**S3**) with a lower HF (*c.a.* 43 T) and an IS near 0.5 mm/s can be attributed to the fictitious intermediate state $Fe^{2.5+}$ due to the fast electron hopping between adjacent Fe^{2+} and Fe^{3+} cations along the B sites of the cubic spinel above the Verwey temperature. As can be seen, the emergence of **S2** is due to the imbalance between Fe^{2+} and Fe^{3+} cations due to the partial substitution of $Fe^{2+}$by Mn^{2+} in the ferrite structure. For the other two measured samples ($x_{Empiric}$=0.23 and 0.37), additional sextets (**S4-S6**) were required. **S4** is attributed to $Fe^{2.5+}$ states where the Fe^{2+} and Fe^{3+} cations have different local environments respect to those in **S3** due to the emergence of inequivalent sites for Fe cations, i.e., the gradual incorporation of Mn^{2+} ions modifies the nearest-neighbor surroundings of Fe cations along the ferrite lattice. In contrast, **S5** and **S6** have large peak widths and HFs below the threshold value (40 T) for FiM behavior, indicating that these contributions encompass a fraction of Fe^{3+} and $Fe^{2.5+}$ sites where the effective magnetic moment is no longer in a blocked FiM state, but it begins to fluctuate at a frequency that is on the order of the inverse of the Mössbauer characteristic time.

The rest of the spectral area contains only a broad quadrupolar doublet **D1** (for the sample with $x_{Empiric}$ = 0.14), or a distribution of HF values **S*n*** (for the samples with $x_{Empiric}$ = 0.23 and 0.37); such distribution is similar in both samples, with IS values centered at 0.3 mm/s, pointing to a dominant contribution from Fe^{3+} cations, consistent with high Mn^{2+} substitution. The relative area of **D1** is small in the $x_{Empiric}$ = 0.14 sample (below 6%), while for the samples with higher Mn^{2+} concentration the

View Article Online
DOI: 10.1039/D5NH00254K

overall contribution from **S*n*** plus **S5** and **S6** sextets drastically increases above 40%. As was mentioned before, these spectral features indicate the occurrence of SPM relaxation, which can be the result of either small MNPs or MNPs with low magnetic anisotropy. Since the three samples exhibit similar size distributions, it is likely that the differences between them arise mostly due to anisotropy effects across the particles. Indeed, the fact that the SPM contribution is more important for the samples with higher Mn^{2+} content strongly suggests that substitution of $Fe^{2+}$by Mn^{2+} in the ferrite lattice induces a decrease of the superexchange interactions[51] that is reflected in lower values of the magnetic anisotropy[54,55] (see next section). Moreover, since XPS results point to a gradient of concentration with large [Mn]/[Fe] molar fraction on the outermost part of the MNPs, it is likely that such SPM relaxation occur preferentially in the surface of the MNPs. Hence, it can be inferred that sextets **S1**-**S4** are associated with the inner part of the MNPs, i.e. the MNP cores exhibit FiM behavior at room temperature. Such finding is further confirmed by estimating the ferrite stoichiometry from the relative area of these four contributions: the [Mn]/[Fe] molar ratio is 0.08, 0.13 and 0.20 for $x_{Empiric}$ = 0.14, 0.23 and 0.37, respectively; these values are very close to those obtained from the 3s XPS data (*cf.* **Figure 2D**), which provides information from the inner part of the MNPs, as has been pointed out.

3.4 Manganese substitution control anisotropy and soft ferrite transition

The influence of Mn^{2+} substitution on the static magnetic properties was analyzed by recording the hysteresis curves at 300 K using a superconducting quantum interference device (SQUID), as described in the experimental section. Magnetization values were normalized to the organic content measured by TGA (**Figure S6** right panel **in the S.I**) and all the magnetic parameters are presented in **Table S5 of the S.I.** Overall, the MNPs showed a superparamagnetic (SPM) behavior at room temperature with negligible remanence or coercitivity (**Figure 3**).The transition from FiM to SPM regime stated by Mössbauer is not evidenced here due to the differences in the time windows for both measurements (~10^{-8} *vs* 10^{2} s). The magnetization values were nearly constant when the Mn^{2+} content varied between $x_{Empiric}$ = 0.14 - 0.70 (80 – 82 $Am^2/kg_{ferrite}$) and decrease for $x_{Empiric}$ = 1.40 (61

View Article Online
DOI: 10.1039/D5NH00254K

$Am^2/kg_{ferrite}$) (**Figure 3A**). Our results are in agreement with the work by Li *et al*., where a series of $Mn_xFe_{3-x}O_4$ MNPs with x = 0.11 up to 0.49, and similar particle and crystal sizes (~ 8.0 nm) showed very similar M_S values and blocking temperatures despite the differences in composition.[12] It is worth nothing that the expected trend of net magnetic moment improvement as a function of Mn^{2+} content is only valid for normal spinel (i = 0), being i the inversion parameter[56–58]. However, the disruption of this trend has been frequently reported due to the presence of crystal defects promoted by the presence of a secondary phase such as wustite[2,3,32] or the oxidation of Mn^{2+} ions to Mn^{3+} and its preference for octahedral sites[59].

The enrichment of Mn^{2+} cations in the outer part of the MNPs (see Figure 2D) could promote a configuration where the spins close to the surface are canted and barely contribute to the M_S in the static regime, explaining the unalterable M_S values with increasing Mn^{2+} content. The heterogeneous allocation of Mn^{2+} cations and the level of Mn^{2+} substitution, could play a major role in reducing the average H_C and M_R. In fact, even when M_S values remain nearly constant across all samples, a slight decrease in the coercitivity value (H_C) was observed while increasing the Mn^{2+} content until $x_{Empiric}$ = 0.70; beyond this point, however, an opposite effect was seen for $x_{Empiric}$ = 1.40. The reduction of H_C via increased Mn^{2+} substitution ultimately led to a decrease in the effective magnetic anisotropy (K_{eff})[60] as also evidenced with Mössbauer measurement, indicating a transition of the MNPs towards soft magnetic behavior (**Figure 3B)**. An exception is the sample with the highest Mn^{2+} content ($x_{Empiric}$ =1.40), where the presence of structural defects, associated with the concomitance of a reduced phase and Mn^{3+} fraction, effectively impacts their magnetic properties.

Similar results were recently reported for cobalt ferrite $Co_xFe_{3-x}O_4$ type MNP, where increasing cobalt content had little effect on M_S across samples, but led to a significant increase of K_{eff}[61]. In summary, considering that all samples exhibited similar average particle and crystallite sizes, and morphologies, the tuneable K_{eff}, the preference of Mn^{2+} for tetrahedral sites and heterogeneous allocations of cations could be the key properties influencing the ultimate magnetic properties[56].

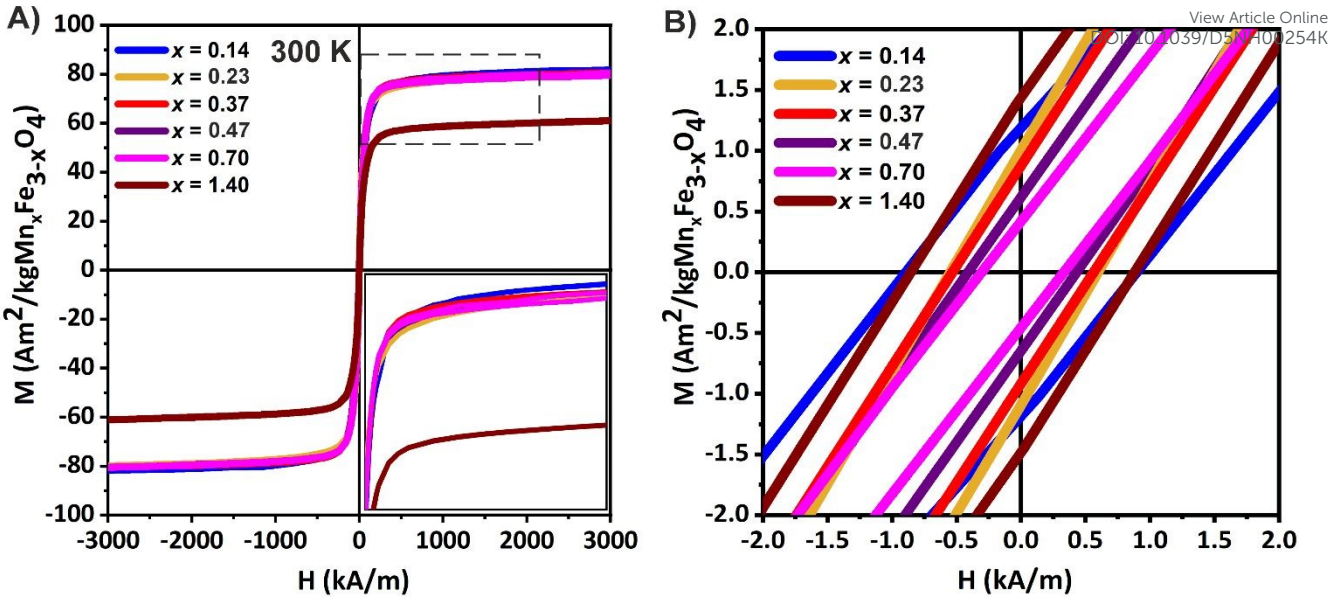

Figure 3. A) Static magnetization cycles recorded at 300 K for the MNPs and **B)** Low field region of the magnetization cycles.

3.5 Mn^{2+} content changes after PMAO polymer coating: Influence on the structural and magnetic properties

The $Mn_xFe_{3-x}O_4$ MNPs were prepared in organic solvents where they remained stabilized by an OA coating, so a subsequent transfer to aqueous phase is required for biomedical applications. To do that, we employed a well-established polymer coating methodology, using an amphiphilic polymer, poly(maleic anhydride-alt-1-octadecene) (PMAO) that intercalates with the OA chains[18]. All MNPs series were transferred to water using the same protocol, rendering MNPs stable in aqueous media for long periods of time. **Table 2** summarizes the characterization of these MNPs coated with PMAO (Mn_x@PMAO) in water. As expected, the transference into water did not affect the shape and core size of the final MNPs as can be seen by TEM (**Figure 4A**), and the hydrodynamic diameter measured by DLS was similar for all MNP (**Table 2**). This indicates a similar transfer to water for all the MNPs regardless of the composition, allowing further comparison between the systems. The successful coating of the MNPs was additionally confirmed by TGA (**Table 2**), as an increase of the organic content between 10 to 24% when compared with samples only coated with OA is in agreement with other reported PMAO-coated MNPs[18,62].

View Article Online
DOI: 10.1039/D5NH00254K

Table 2. Summary of the physico-chemical properties of Mn_x@PMAO MNPs. Hydrodynamic radius (D_{DLS}) is presented in terms of intensity distribution.

Samples	empirical *x* value before PMAO	Empirical *x* value after PMAO	Measured formula	D_{TEM} (nm±σ)	D_{DLS} (nm±SD)	Z potential (mV±SD)	Organic content (%)
Mn_x@PMAO	0.14	0.07	$Mn_{0.07}Fe_{2.93}O_4$	12.9 ± 1.9	51.1±1.6	-38.1±7.2	39.9
	0.23	0.20	$Mn_{0.20}Fe_{2.80}O_4$	13.9 ± 2.1	65.5±0.7	-37.7±6.1	27.3
	0.37	0.30	$Mn_{0.30}Fe_{2.70}O_4$	14.6 ± 2.3	66.5±1.9	-31.2±4.8	23.6
	0.47	0.40	$Mn_{0.40}Fe_{2.60}O_4$	14.3 ± 1.2	66.6±0.4	-39.6±8.2	32.0
	0.70	0.60	$Mn_{0.60}Fe_{2.40}O_4$	14.4 ± 1.8	69.4±2.3	-34.3±6.8	28.4
	1.40	1.10	$Mn_{1.10}Fe_{1.90}O_4$	13.6 ± 1.3	66.5±1.8	-32.3±4.2	34.6

Surface modification can play a major role in the redistribution of cations, ultimately modifying the final composition of the spinel structure and its functionality[63,64]. To study the influence of PMAO coating on the composition and, thus, the structural and magnetic properties, the samples were characterized after coating by ICP-OES, FT-IR and XRD. From the ICP-OES results, we confirmed that Mn^{2+} ions leached out from the MNPs after PMAO coating (**Table 2**), as previously reported after DMSA or dopamine coating[16]. Mn^{2+} losses ranged from 13.0 to 21.4% of the initially incorporated amount across samples, except for the sample containing the lowest content of Mn^{2+}, which exhibited a loss of nearly 50% of its Mn^{2+} ions. This trend aligns with the XPS data (**Figure 2D**).

The stability of cations occupying surface sites also depends on their interaction with the surface ligand and/or the solvent[56]. **Figure 4B** shows the FT-IR spectra of the selected MNPs with the lowest ($x_{Empiric}$ = 0.07) and the highest Mn^{2+} content ($x_{Empiric}$ = 1.10) after PMAO coating. In region I, the signals of ν(C–H) stretching mode belonging to the OA anchored to the surface of MNPs dominate, being more intense for the sample with the highest percentage of OA ($x_{Empiric}$ = 0.07), as also confirmed by TGA. Next, region II is dominated by two broad bands that correspond to $\nu_{as}(COO^-)$ and $\nu_s(COO^-)$ modes of metal carboxylates, indicating the successful polymer coating. The intense band that appears in region III is characteristic of lattice Fe-O vibrations in spinel ferrites. Interestingly, as Mn^{2+} content increased, this band showed a left shift, indicating the modification of Fe-O bond lengths and the rearrangement

View Article Online
DOI: 10.1039/D5NH00254K

of the oxygen sublattice to accommodate different cation distributions among the octahedral and tetrahedral sites, which was affected by PMAO coating[56]. In agreement with this, a gradual shift in the mean peak (311) position can also be seen by comparing the XRD patterns of samples before and after polymer coating, while the spinel ferrite structure was maintained (**Figure 4C**).

The effect of polymer coating on the magnetic properties was evaluated at 5 K and 300 K, with results summarized in **Table 3**. In agreement with initial oleic acid coated MNPs behavior, both the H_C and the M_R decreased to near zero values at RT, indicating that the SPM regime was preserved after surface modification. The M_S values were slightly higher (85.0 – 89.0 $Am^2/kg_{ferrite}$) than initial MNPs (See Section 3.4, Figure 3) or Fe_3O_4 MNPs (82 Am^2/kg) obtained under the same synthetic procedure at 300 K (**Figure 4D**). Changes in the magnetic properties after surface modification have been previously reported when using different polymers such as triethyleneglycol (TEG) and polyethyleneglycol (PEG), attributed to the reduction of spin canting effect[65,66]. However, this does not fully apply in our case, as PMAO polymer is not directly coordinated to the iron ions but rather intercalated in the OA chains; nevertheless, PMAO coating could be associated with ion leaching and subsequent cation redistribution on the MNPs surface[60,67] which is relevant for applications dependent on surface properties such as AC hysteresis and relaxometry[63].

Table 3. Magnetic parameters of Mn_x@PMAO samples at 300 K and 5 K.

Samples	300 K			5 K				
Mn_x@PMAO	**M_S (Am^2/kg)**	**H_C (kA/m)**	**M_R (Am^2/kg)**	**M_S (Am^2/kg)**	**H_C (kA/m)**	**M_R (Am^2/kg)**	**[a]H_K (kA/m)**	**K_{eff} ($10^5 J/m^3$)**
$Mn_{0.07}Fe_{2.93}O_4$	85	2.6	16	100	22.9	40	100	3.9
$Mn_{0.30}Fe_{2.70}O_4$	86	2.6	16	101	20.5	39	80	3.2
$Mn_{0.40}Fe_{2.60}O_4$	87	2.6	17	102	19.4	37	72	2.9
$Mn_{0.60}Fe_{2.40}O_4$	89	2.6	17	107	16.6	44	64	2.7
$Mn_{1.10}Fe_{1.60}O_4$	66	2.6	5	85	24.1	18	100	3.3
Fe_3O_4	82	2.6	12	92	22.9	34	80	2.9

[a]Determined as the field at which the magnetization of the magnetized and the demagnetized branches differs in 3% of M_S[60].

View Article Online
DOI: 10.1039/D5NH00254K

The effective anisotropy constant (K_{eff}) of the different MNP@PMAO samples were estimated from the formula $Keff = \frac{Ms*Hk}{2}$, M_S and H_K being measured at 5 K following Stoner and Wohlfarth model[68,60]. The obtained values (**Table 3**) confirmed a decrease in K_{eff} from 3.9 to 2.7 x 10^5 J/m^3 as Mn^{2+} content increased up to $x_{Empiric}$ = 0.60 and an increase for samples with $x \geq 0.60$, confirming the direct correlation between H_C and Mn^{2+} content. K_{eff} values are approximate due to assumptions of full saturation, negligible temperature variation between 0–5 K, and limited interparticle interaction effects at high fields. It is noticeable that K_{eff} for $Mn_{0.60}Fe_{2.40}O_4$ is close to the values reported for $MnFe_2O_4$ MNPs (1-2 × 10^5 J/m^3)[60,69,70], which highlights the crucial impact of Mn^{2+} content on the effective anisotropy of the samples.

View Article Online
DOI: 10.1039/D5NH00254K

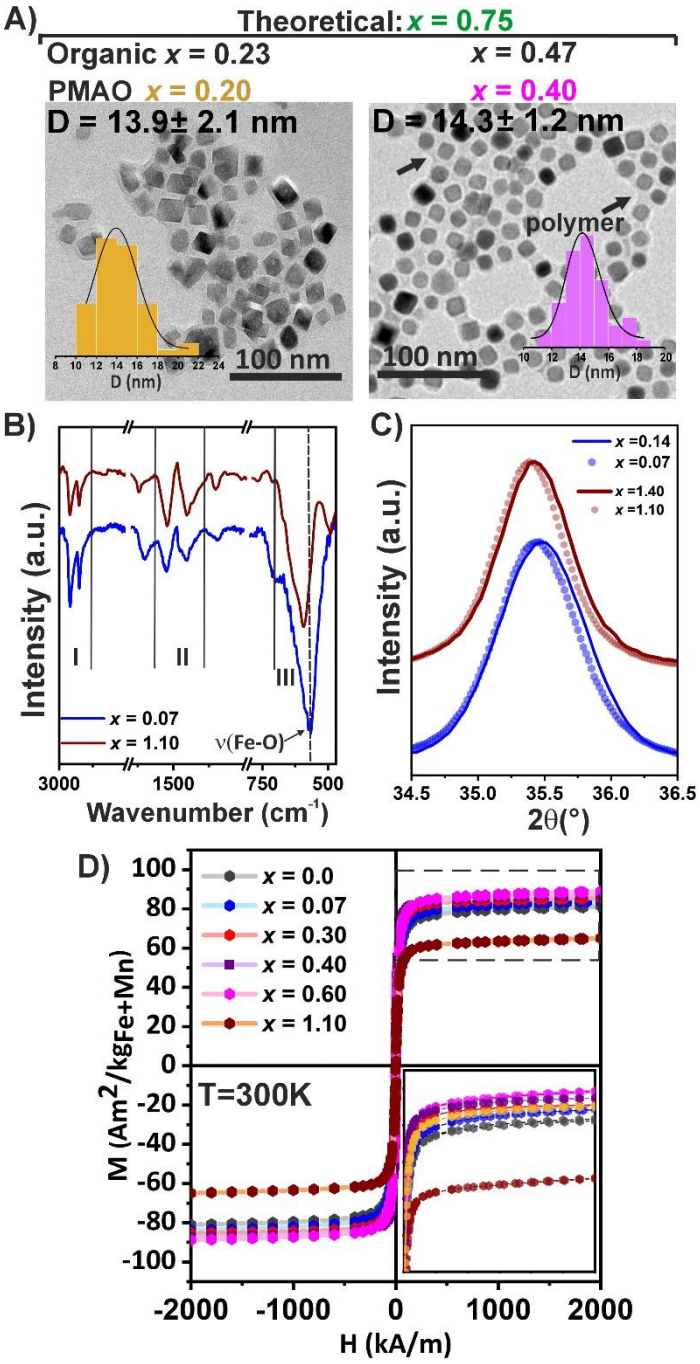

Figure 4. Influence of PMAO coating on structural and magnetic properties of $Mn_xFe_{3-x}O_4$ MNPs. **A)** TEM images of selected Mn_x@PMAO samples and their corresponding histogram size distribution. Theoretical and empirical *x* values obtained in organic and aqueous media are shown. **B)** FT-IR spectra for Mn_x@PMAO with $x_{Empiric}$ = 0.07 and 1.10, respectively. **C)** Comparison between XRD patterns with initial composition (organic) of $x_{Empiric}$ = 0.14, and 1.40, and after water transference $x_{Empiric}$ = 0.07, and 1.10, respectively. **D)** Magnetization cycles of Mn_x@PMAO serie ($x_{Empiric}$ = 0.07 up to 1.10) compared with Fe_3O_4 (*x* = 0.0) obtained under the same synthetic procedure at 300 K.

View Article Online
DOI: 10.1039/D5NH00254K

3.6 Tuning heating performance by changing Mn^{2+} content.

The influence of the Mn^{2+} content on the heating capability of the Mn_x@PMAO MNPs was studied by two methods: calorimetry and AC magnetometry. Low- and high-frequency measurements were conducted at magnetic ion concentrations of 2 mg_{Fe+Mn}/mL or 1 mg_{Fe+Mn}/mL, respectively.

3.6.1 Calorimetric measurements

Figures 5A and **B** show the heating performance at different magnetic field intensities ranging from H = 3.8 up to 44.6 kA/m under a low (f = 155 kHz) and a high frequency (f = 763 kHz), respectively. In general, samples with $x_{Empiric}$ = 0.07 up to 0.60 showed better heating performance than the corresponding iron oxide (x = 0.0) MNPs with similar sizes and shapes obtained under the same synthetic procedure. As expected for SPM MNPs, the SLP values increased with the intensity of the applied magnetic field and the Mn^{2+} content (until $x_{Empiric}$ = 0.60), being always higher under the high-frequency regime (**Figure 5B**). However, for samples with $x_{Empiric}$ = 1.10, negligible SLP values were obtained under safe clinical conditions (delimited with a red dotted line). The largest SLP value was recorded for the sample with $x_{Empiric}$ = 0.60 under both regimes, in agreement with their improved magnetic properties and low magnetic anisotropy confirmed by the previous data. The heating curve dependence of the applied frequency (155, 388, 637, and 763 kHz) under a fixed H = 16.8 kA/m also showed a linear increase (**Figure S7 in the S.I**). One can conclude that as structural defects and the presence of Mn^{3+} species became significant ($x_{Empiric}$ = 1.10), a strong deterioration of M_S values was observed, and therefore, measurable heating dissipation was only possible under high magnetic field intensity exposure (**Figure 5A-B**). Several works have reported the detrimental effect of crystal defects (strains, antiphase boundaries, etc.) on heat production[3,71,72]. This parameter is strictly linked to the synthetic protocol used for the preparation of MNPs and needs to be considered in terms of nanoheater optimization for MHT.

View Article Online
DOI: 10.1039/D5NH00254K

The SLP computed values for high and low-frequency regimes appear in **Table S6-S7 in the S.I.** These SLP values shown in **Figure 5A-B** were fitted with a power law $SLP = \varphi H^n$, being φ the mass concentration of the MNPs in the colloid, H the amplitude of the applied field, and n the power exponent (between 1.99 and 1.09) within the linear response theory (LRT)[73,74]. As low-frequency measurements did not produce accurate fitting, values were not considered. However, under a fixed frequency of 763 kHz (**Figure 5B**), the quadratic field dependence of the SLP is fulfilled under all the range of magnetic fields tested, and it is independent of the composition (**Table S7 in the S.I.**). From this data, we can conclude that the variation of the composition (maintaining similar size and shape) with the amplitude of the magnetic field only affects the regime of dissipation of the MNP if the incorporation of Mn^{2+} produces structural defects and/or concomitate with different Mn species like Mn^{3+}. On the contrary, even with a very different Mn^{2+} content but without any impact on the average structural-magnetic properties, the heat dissipation regimen is warranted within the SPM regime. Still, the SLP values can be successfully tuned with the Mn^{2+} increase.

Magnetic relaxation process of MNPs dispersed in liquids results from individual or combination of Néel and Brown relaxation mechanisms[73,75]. To unveil between the predominance of Néel and Brown relaxation to produce heat over the anisotropy energy barrier, we tuned the viscosity of the medium containing the MNPs. Specifically, our best nanoheater ($x_{Empiric}$ = 0.60) was dispersed in water with increasing final amounts (% v/v) of glycerol (2% and 50%, viscosity range up to ~ 15 mPa.s[75]) and measured by calorimetry at a field intensity of 16.8-28.8 kA/m and f = 763 kHz. We observed that the SLP values remained unaltered when the viscosity of the media was changed (**see Figure S8 in S.I.**), suggesting that the Néel relaxation process is the predominant mechanism[61,76]. This finding aligns with other works reporting that Fe_3O_4 MNPs of 16 nm and 14 nm in water and in glycerol, respectively, are needed to maintain the predominance of Néel relaxation mechanism under a broad range of frequencies (100 kHz to 1 MHz)[61,77]. In contrast, for more advanced compositions such as cobalt ferrite, the Néel relaxation mechanism predominates only within a size range of 6-10 nm[61,78]. In our case the

View Article Online
DOI: 10.1039/D5NH00254K

predominance of Néel relaxation across compositions and in the range of 13- 15 nm just by controlling K_{eff} is a crucial strategy for the design of soft ferrite MNPs as heat mediators in complex environments such as tumors, where MNP tends to aggregate, potentially compromising their magnetic properties[79–83].

View Article Online
DOI: 10.1039/D5NH00254K

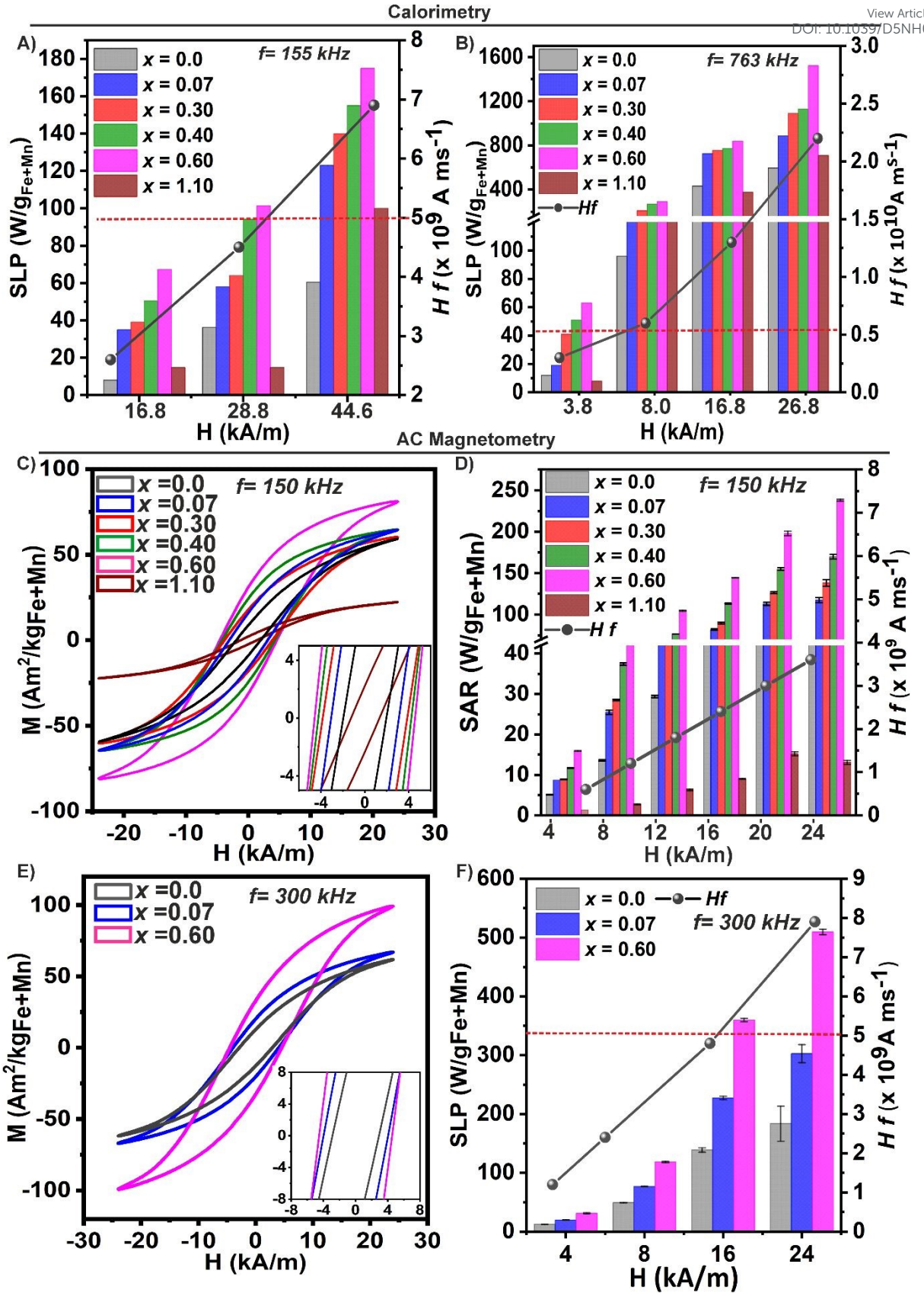

Figure 5. Effect of Mn^{2+} content on the heating efficiency of $Mn_xFe_{3-x}O_4$ MNPs. SLP values obtained by calorimetric method for $Mn_xFe_{3-x}O_4$ MNPs with a fixed frequency of **A)** f=155 kHz and **B)** f=763 kHz under field intensity (H) ranging from 3.8 up to 44.6 kA/m. **C)** Dynamic magnetization curves obtained at 150 kHz and 24 kA/m for samples with $x_{Empiric}$ = 0.0, 0.07, 0.30, 0.40, 0.60, and 1.10. Inset:

Magnification of low field region. **D)** SAR values of the correspondent samples (with $x_{Empiric}$ = 0.0 up to 1.10). **E)** Dynamic magnetization curves obtained at 300 kHz and 24 kA/m of samples with $x_{Empiric}$ = 0.07 and 0.70, respectively, compared to samples without Mn^{2+} (x = 0.0). Inset: Low field region. **F)** SAR value of samples measured in E). Black dots represent the *Hf* values for each condition tested. Safe clinic *Hf* values are delimited with a red dotted line.

3.6.2 AC magnetization measurements

AC magnetic hysteresis loops were measured for MNPs dispersed in solutions with different Mn^{2+} content by AC magnetometry to obtain SAR values at 150 and 300 kHz and field intensities (H_{ac}) ranging from 4 to 24 kA/m (**Figure 5C-E)**. In general, the evolution of SAR(H_{ac}) showed similar trends compared with the calorimetric method. As Mn^{2+} content raised (until $x_{Empiric} \leq 0.60$), the areas of the cycles increased under both frequencies at a field amplitude of 24 kA/m, while the opposite trend was observed for samples with $x_{Empiric}$ = 1.10 (**Figure 5C and E**). The evolution of the AC hysteresis loops as a function of the H_{ac} (4 up to 24 kA/m) for selected samples ($x_{Empiric}$ = 0.07, 0.60, and 1.10) is shown in **Figure S9 in the S.I.** At 150 kHz, $x_{Empiric}$ = 1.10 displayed low SAR under all amplitudes tested, exhibiting 'S'-shaped hysteresis loops curve characteristic of 'hard ferrite-type' materials[84], whereas, for the rest of samples, the heating efficiency rises quickly depending on the Mn^{2+} content consistent with the 'soft-ferrite' type of MNPs (**Figure 5C-D** and **Table S8-9 in the S.I.)**. Interestingly, field amplitude-dependent SAR appeared to be linear, with values reaching a plateau with field amplitudes above the threshold of ≥ 20 kA/m for MNPs ($x_{Empiric}$ = 0.0 up to 0.60), indicating a possible saturation (**Figure S10A in the S.I.**).

Figure 5E depicts the AC hysteresis loops at 300 kHz for samples with $x_{Empiric}$ = 0.0, 0.07, and 0.60, also showing a dependence on the Mn^{2+} content. The sample with $x_{Empiric}$ = 0.60 presented the largest opening of the AC hysteresis loops, and thus, a SAR value of about 510 W/g_{Fe+Mn}, whereas Fe_3O_4 MNPs in a similar range of sizes showed a smaller area (SAR= 184 W/g_{Fe+Mn}) under the same AMF conditions (300 kHz, 24 kA/m) (**Figure 5F and Table S9 in the S.I.**). Linear SAR(H_{ac}) dependence was maintained as in the case of 150 kHz measurement with a plateau deviation with amplitude ≥ 20 kA/m (**Figure S10B in the S.I.**).

View Article Online
DOI: 10.1039/D5NH00254K

Aiming to compare both methods, we selected very near low frequencies, 155 kHz for the calorimetric method and 150 kHz for AC magnetometry at a fixed *H* of 16.8 kA/m. Considering our best nanoheater ($x_{Empiric}$ = 0.60), we obtained a SLP = 67.3 W/g_{Fe+Mn} by calorimetry compared with SAR =144.5 W/g_{Fe+Mn} by magnetometry. The differences could be attributed to the non-adiabatic conditions employed for calorimetry measurements, resulting in lower Dt/dt depending on the thermal exchange of MNP suspension with the surrounding media[85]. However, if we compared the results depicted in **Figure 5A** and **D** it is evident that the heating capacity tendency as a function of the Mn^{2+} content is maintained under both methods, showing their complementarity.

3.7 MNP-cell interaction

Recently we reported that tuning Mn^{2+} composition is crucial to modulate the amount of reactive oxygen species (ROS) produced under magnetic hyperthermia to enhance regeneration in the invertebrate model organism *Hydra vulgaris*[86]. To study the future potential of $Mn_xFe_{3-x}O_4$ MNPs for cancer treatment, we selected two MNPs with different heating capacity ($x_{Empiric}$ = 0.07 and 0.60). To confer improved stability in biological media and target tumoral cells, the samples were functionalized with glucose molecules[19]. The cytotoxicity of $Mn_{0.07}Fe_{2.93}O_4$ and $Mn_{0.60}Fe_{2.40}O_4$ MNPs coated with glucose at different concentrations (ranging from 0 to 150 μg/mL) was evaluated by MTT assay, a well-known colorimetric method used to assess cell metabolic activity as an indicator of cell viability. Cell viability of MIA PaCa-2 cell line was greater than 90% for both systems ($x_{Empiric}$ = 0.07 and 0.60, respectively) after 24 h of treatment, suggesting the absence of cell cytotoxicity and the biocompatibility of MNPs up to 150 μg/mL **(Figure 6A-B)**. These results are consistent with previous published data where low levels of toxicity are reported in different cell lines for manganese iron oxide nanoparticles[16,87,88]. Similarly, these results mirror those obtained in vivo in Hydra vulgaris, where none of both MNPs resulted toxic [90]. Then, we assessed the internalization of $Mn_xFe_{3-x}O_4$ in MIA PaCa-2 cell line by fluorescence microscopy and ICP-OES technique. As can be seen in **Figure 6C**, large amounts of both $Mn_xFe_{3-x}O_4$ MNPs appeared internalized inside the cells as red spots in comparison

View Article Online
DOI: 10.1039/D5NH00254K

with the control (cells without MNPs), suggesting high cellular uptake after 24 h of treatment. This result is important for applications like classical magnetic hyperthermia where high internalization of iron is required to achieve therapeutical heat. To confirm that, intracellular iron content was measured by ICP-OES. After 24 h of treatment, the amount of intracellular Fe was 8 and 15 pg/cell for $Mn_{0.07}Fe_{2.93}O_4$ and $Mn_{0.60}Fe_{2.40}O_4$ MNPs, respectively. The difference between samples could be attributed to a different amount of glucose functionalized on the MNPs surface, or a diverse stability in biological media. Further studies to elucidate the dependence between nanoparticle composition and cellular internalization are still needed.

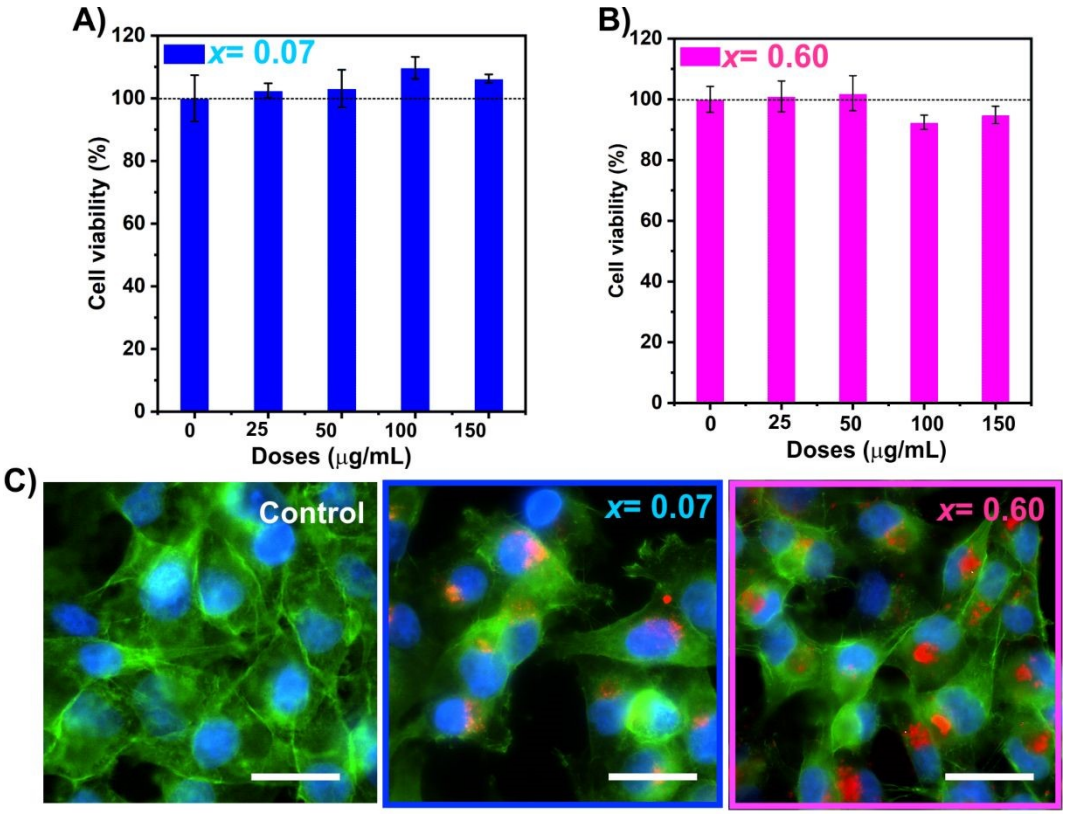

Figure 6. A-B) Viability assay in MIA PaCa-2 cell line loaded $Mn_xFe_{3-x}O_4$ MNPs, with x = 0.07 and 0.60; respectively. **C)** Fluorescence images taken after 24 h of incubation with 100 μg/mL of TAMRA-labelled MNPs in MIA PaCa-2 cells. Nuclei (blue), Green (F-actin) and Red (MNPs). Scale bar = 20 μm.

View Article Online
DOI: 10.1039/D5NH00254K

Conclusions

Besides shape and size, the MNPs composition is a critical parameter to tune heating efficiency. In this study, we investigated the effects of manganese content on the structural, magnetic and heating response of $Mn_xFe_{3-x}O_4$ MNPs before and after water transference. Our study reveals a compositional gradient in the Mn/Fe atomic ratios across the MNPs, with the surface layers being enriched in Mn^{2+} relative to the deeper core regions. This heterogeneity becomes more pronounced as the Mn^{2+} substitution level decreases. The data suggest that Mn ions primarily incorporate into the ferrite structure starting from the outermost layers, gradually extending toward the interior of the nanoparticle. The surface of the nanoparticles, enriched with Mn^{2+}, likely exhibits a SPM relaxation, while the inner core remains predominantly FiM. We have successfully tuned the K_{eff} by varying the Mn^{2+} content in the samples with $x_{Empiric} \leq 0.70$ while keeping the M_S and crystallite sizes relatively constant. In contrast, higher Mn^{2+} content ($x_{Empiric} = 1.40$) exhibited additional secondary crystalline phase, strain defects, and presence of Mn^{3+} species, affecting the M_S values although the final crystallite size remained also unalterable. Water transference by PMAO coating provoked ion leaching that clearly changed the initial composition of the MNPs, but average static magnetic properties were maintained. The heating efficiency was effectively tuned by changing the Mn^{2+} content, being the ferrites with $x_{Empiric} = 0.60$, the ones with the optimal Mn^{2+} concentration and anisotropy that maximizes SLP. Néel relaxation process was the predominant mechanism to produce heat for our set of MNPs. Importantly, cell viability remained greater than 90% for Mn^{2+} tested concentration, suggesting that this system is safe after 24 hours of treatment. Essentially, our study highlights the importance of fine-tuning these properties and presents a valuable framework for advancing magnetic hyperthermia through targeted nanoparticle design. Moreover, the ability to control magnetic anisotropy and heating performance through Mn^{2+} content highlights the potential of these nanoparticles for biomedical applications, including localized in vivo hyperthermia treatments, as recently demonstrated in *Hydra vulgaris* [90].

View Article Online
DOI: 10.1039/D5NH00254K

View Article Online
DOI: 10.1039/D5NH00254K

Author contributions

O.F.O. Investigation, XPS measurement and analysis, Data curation, Writing original draft

G. T. Investigation, Biological experiment, Data curation, Writing original draft.

F. J. T. Resources, review & editing

J. G. O. Investigation, review & editing

J. R. Mossbauer measurement and analysis. Writing original draft

M. M. Conceptualization, Funding acquisition, Project administration, Supervision and review & editing

S.DS.F. Conceptualization, Investigation, Data curation, Formal analysis, Writing original draft; and review & editing

Conflicts of interest

There are no conflicts to declare.

ACKNOWLEDGMENTS

The authors would like to acknowledge the use of Advanced Microscopy Laboratory (Universidad de Zaragoza), for access to their instrumentation and expertise and the use of Servicio General de Apoyo a la Investigación-SAI, Universidad de Zaragoza. Likewise, the authors thank LNCAE (Laboratorio Nacional de Conversión y Almacenamiento de Energía) from the IPN (Instituto Politécnico Nacional) for access to its XPS experimental facility. We also thank Professor M. del Puerto Morales (MaMBIO Group, ICMM), Professor Edilso Reguera (CICATA-Legaria, IPN) and Dr. Raluca Fratila (Bionanosurf group, INMA-CSIC).

Funding

S.DS.F. acknowledges Marie Skłodowska-Curie Postdoctoral Fellowships (HORIZON-MSCA-2021-PF-01-01, Grant agreement No 101064735) funded by the European Union. This work has received funding from the European Research Council (ERC) under the European Union's Horizon 2020 research and innovation program (Grant agreement No.853468), MCIN/AEI/10.13039/501100011033 and FSE+ (PID2021-122508NB-I00) and project CNS2022-135700 funded by MICIU/AEI

/10.13039/501100011033 and the European Union NextGenerationEU/PRTR. The authors would like to acknowledge Fondo Social del Gobierno de Aragón (grupo DGA E15_23R) and MCIN with funding from European Union NextGenerationEU (PRTR-C17.I1) promoted by the Government of Aragon. The project CONAHCyT LNC-2023-95 partially supported this study. Ayuda CEX2023-001286-S financiada por MICIU/AEI /10.13039/501100011033

Footnotes

Supplementary information is available: Experimental conditions employed for the synthesis of the two series of MNPs. TEM characterization for samples with equal compositions but varying the ratio OA/Fe-Mn, EDX spectrums, lattice strain calculation, a section dedicated to curve fitting of the high-resolution spectra of Mn 3s and Fe 3s signals and proper quantification of Mn/Fe ratios, XPS of high resolution spectra, TGA analysis, magnetic properties of oleic acid coated MNPs at 300K, heating curves under different frequencies, SAR evolution *vs.*glycerol content, and SAR values by AC magnetometry.

ORCID iDs

S.DS.F. 0000-0002-7660-966X

O.F.O. 0000-0002-0092-089X

G. T. 0000-0001-6604-0097

F. J. T. 0000-0002-2466-6208

J. G. O.

J.R

M. M. 0000-0002-2861-2469.

References

View Article Online
DOI: 10.1039/D5NH00254K

1 H. Gavilán, S. K. Avugadda, T. Fernández-Cabada, N. Soni, M. Cassani, B. T. Mai, R. Chantrell and T. Pellegrino, *Chem Soc Rev*.

2 L. Yang, L. Ma, J. Xin, A. Li, C. Sun, R. Wei, B. W. Ren, Z. Chen, H. Lin and J. Gao, *Chemistry of Materials*, 2017, **29**, 3038–3047.

3 S. Del Sol Fernández, O. F. Odio, P. M. Crespo, E. O. Pérez, G. Salas, L. Gutiérrez, M. del P. Morales and E. Reguera, *The Journal of Physical Chemistry C*, 2022, **126**, 10110–10128.

4 S. S. Phalake, M. S. Lad, K. V Kadam, S. A. M. Tofail, N. D. Thorat and V. M. Khot, *ACS Omega*, 2022, **7**, 44187–44198.

5 D. Li, H. Yun, B. T. Diroll, V. V. T. Doan-Nguyen, J. M. Kikkawa and C. B. Murray, *Chemistry of Materials*, 2016, **28**, 480–489.

6 N. Zufelato, V. R. R. Aquino, N. Shrivastava, S. Mendanha, R. Miotto and A. F. Bakuzis, *ACS Appl Nano Mater*, 2022, **5**, 7521–7539.

7 X. Lasheras, M. Insausti, J. M. de la Fuente, I. G. de Muro, I. Castellanos-Rubio, L. Marcano, M. L. Fernández-Gubieda, A. Serrano, R. Martin-Rodriguez, E. Garaio and others, *Dalton Transactions*, 2019, **48**, 11480–11491.

8 Z. Yan, A. Chaluvadi, S. FitzGerald, S. Spence, C. Bleyer, J. Zhu, T. M. Crawford, R. B. Getman, J. Watt, D. L. Huber and others, *Nanoscale Adv*, 2022, **4**, 3957–3965.

9 A. Doaga, A. M. Cojocariu, W. Amin, F. Heib, P. Bender, R. Hempelmann and O. F. Caltun, *Mater Chem Phys*, 2013, **143**, 305–310.

10 L. T. Lu, N. T. Dung, L. D. Tung, C. T. Thanh, O. K. Quy, N. V Chuc, S. Maenosono and N. T. K. Thanh, *Nanoscale*, 2015, **7**, 19596–19610.

11 X. Yu, T. Yang, C. Lv, L. Wang, R. Liu, D. Tian, S. He and others, *J Alloys Compd*, 2023, **937**, 168291.

12 D. Li, H. Yun, B. T. Diroll, V. V. T. Doan-Nguyen, J. M. Kikkawa and C. B. Murray, *Chemistry of Materials*, 2016, **28**, 480–489.

13 Z. Yan, A. Chaluvadi, S. FitzGerald, S. Spence, C. Bleyer, J. Zhu, T. M. Crawford, R. B. Getman, J. Watt, D. L. Huber and others, *Nanoscale Adv*, 2022, **4**, 3957–3965.

14 R. Otero-Lorenzo, E. Fantechi, C. Sangregorio and V. Salgueiriño, *Chemistry--A European Journal*, 2016, **22**, 6666–6675.

15 L. H. Nguyen, N. X. Phuc, D. H. Manh, N. H. Nam, N. X. Truong, N. V Quynh, P. T. Phong and P. H. Nam, *J Electron Mater*, 2021, **50**, 5318–5326.

16 D. Garc\'\ia-Soriano, R. Amaro, N. Lafuente-Gómez, P. Milán-Rois, Á. Somoza, C. Nav\'\io, F. Herranz, L. Gutiérrez and G. Salas, *J Colloid Interface Sci*, 2020, **578**, 510–521.

17 H. Zeng, P. M. Rice, S. X. Wang and S. Sun, *J Am Chem Soc*, 2004, **126**, 11458–11459.

18 M. Moros, B. Pelaz, P. López-Larrubia, M. L. Garc\'\ia-Martin, V. Grazú and J. M. de La Fuente, *Nanoscale*, 2010, **2**, 1746–1755.

19 M. Moros, B. Hernaez, E. Garet, J. T. Dias, B. Saez, V. Grazu, A. Gonzalez-Fernandez, C. Alonso and J. M. de la Fuente, *ACS Nano*, 2012, **6**, 1565–1577.

20 K. R. Desai, S. T. Alone, S. R. Wadgane, S. E. Shirsath, K. M. Batoo, A. Imran, E. H. Raslan, M. Hadi, M. F. Ijaz and R. H. Kadam, *Physica B Condens Matter*, 2021, **614**, 413054.

21 J. T. Dias, M. Moros, P. Del Pino, S. Rivera, V. Grazú and J. M. de la Fuente, *Angewandte Chemie*, 2013, **125**, 11740–11743.

22 B. Mehdaoui, J. Carrey, M. Stadler, A. Cornejo, C. Nayral, F. Delpech, B. Chaudret and M. Respaud, *Appl Phys Lett*.

23 G. Cotin, F. Perton, C. Petit, S. Sall, C. Kiefer, V. Begin, B. Pichon, C. Lefevre, D. Mertz, J.-M. Greneche and others, *Chemistry of Materials*, 2020, **32**, 9245–9259.

24 W. Baaziz, B. P. Pichon, S. Fleutot, Y. Liu, C. Lefevre, J.-M. Greneche, M. Toumi, T. Mhiri and S. Begin-Colin, *The Journal of Physical Chemistry C*, 2014, **118**, 3795–3810.

25 C. Moya, X. Batlle and A. Labarta, *Physical Chemistry Chemical Physics*, 2015, **17**, 27373–27379.

26 Q. Song, Y. Ding, Z. L. Wang and Z. J. Zhang, *Chemistry of Materials*, 2007, **19**, 4633–4638.

27 F. J. Douglas, D. A. MacLaren and M. Murrie, *RSC Adv*, 2012, **2**, 8027–8035.

28 S. Carregal-Romero, A. B. Miguel-Coello, L. Mart\'\inez-Parra, Y. Fernández-Afonso, S. Plaza, L. Gutierrez, P. Lecante, Z. Blasco-Iturri, L. Fadón, A. C. Almansa-Garc\'\ia and others, .

29 S. D. Oberdick, A. Abdelgawad, C. Moya, S. Mesbahi-Vasey, D. Kepaptsoglou, V. K. Lazarov, R. F. L. Evans, D. Meilak, E. Skoropata, J. van Lierop and others, *Sci Rep*, 2018, **8**, 1–12.

30 A. Ullrich, M. M. Rahman, P. Longo and S. Horn, *Sci Rep*, 2019, **9**, 1–9.

31 A. Lak, D. Niculaes, G. C. Anyfantis, G. Bertoni, M. J. Barthel, S. Marras, M. Cassani, S. Nitti, A. Athanassiou, C. Giannini and others, *Sci Rep*, 2016, **6**, 33295.

32 A. Lak, M. Cassani, B. T. Mai, N. Winckelmans, D. Cabrera, E. Sadrollahi, S. Marras, H. Remmer, S. Fiorito, L. Cremades-Jimeno and others, *Nano Lett*, 2018, **18**, 6856–6866.

33 G. K. Williamson and W. H. Hall, *Acta metallurgica*, 1953, **1**, 22–31.

34 P. Monisha, P. Priyadharshini, S. S. Gomathi and K. Pushpanathan, *Journal of Physics and Chemistry of Solids*, 2021, **148**, 109654.

35 C. S. Fadley, D. A. Shirley, A. J. Freeman, P. S. Bagus and J. V. Mallow, *Phys. Rev. Lett.*, 1969, **23**, 1397–1401.

36 S. Hüfner and G. K. Wertheim, *Phys. Rev. B*, 1973, **7**, 2333–2336.

37 G.-H. Gweon and J.-G. S.-J. Park, *Phys. Rev. B.*, 1993, **48**, 7825–7835.

38 R. Gupta and D. Sharma, *ACS Appl Nano Mater*, 2020, **3**, 2026–2037.

39 I. V Chernyshova, S. Ponnurangam and P. Somasundaran, *J Am Chem Soc*, 2011, **133**, 9536–9544.

40 J. F. van Acker, *Phys. Rev. B*, 1988, **37**, 6827--6834.

41 J. C. Carver, G. K. Schweitzer and Thomas A. Carlson, *J. Chem. Phys.*, 1972, **57**, 973–982.

42 V. R. Galakhov, M. Demeter, S. Bartkowski, M. Neumann, N. A. Ovechkina, E. Z. Kurmaev, N. I. Lobachevskaya, Y. M. Mukovskii, J. Mitchell and D. L. Ederer, *Phys Rev B*, 2002, **65**, 113102.

43 G. C. Allen, S. J. Harris, J. A. Jutson and J. M. Dyke, *Appl Surf Sci*, 1989, **37**, 111–134.

44 A. Kumar, B. N. Mahanty, A. Rawat, R. Muhammad, R. K. Panigrahi, D. Pradhan and P. Mohanty, *Energy & Fuels*, 2023, **37**, 6810–6823.

45 S. Güner, A. Baykal, Md. Amir, H. Güngüneş, M. Geleri, H. Sözeri, S. E. Shirsath and M. Sertkol, *J Alloys Compd*, 2016, **688**, 675–686.

46 J. B. Goodenough, *Phys. Rev.*, 1955, **100**, 564–573.

47 Eeva-Kaarina Viinikka and Yngve Öhrn, *Phys. Rev.*

48 S. Tanuma, C. J. Powell and D. R. Penn, *Surface and Interface Analysis*, 1991, **17**, 911–926.

49 P. P. Bakare, M. P. Gupta, S. K. Date and A. P. B. Sinha, *Proceedings of the Indian Academy of Sciences - Chemical Sciences*, 1984, **93**, 1349–1359.

50 K. S. Al-Rashdi, H. M. Widatallah, F. Al Ma  Mari, O. Cespedes, M. Elzain, A. Al-Rawas, A. Gismelseed and A. Yousif, *Hyperfine Interact*, 2018, **239**, 1–11.

51 G. A. Sawatzky, F. Van Der Woude and A. H. Morrish, *Phys. Rev.*, 1969, **187**, 747–757.

52 F. L. Deepak, M. Bañobre-López, E. Carbó-Argibay, M. F. Cerqueira, Y. Piñeiro-Redondo, J. Rivas, C. M. Thompson, S. Kamali, C. Rodríguez-Abreu, K. Kovnir and Y. V Kolen'ko, *The Journal of Physical Chemistry C*, 2015, **119**, 11947–11957.

53 D. G. Rancourt and J. Y. Ping, *Nucl Instrum Methods Phys Res B*, 1991, **58**, 85–97.

54 R. Gerber and G. Elbinger, *Journal of Physics C: Solid State Physics*, 1970, **3**, 1363.

55 A. Broese Van Groenou, J. A. Schulkes and D. A. Annis, *J. Appl. Phys.*, 1967, 1133–1134.

56 K. R. Sanchez-Lievanos, J. L. Stair and K. E. Knowles, *Inorg Chem*, 2021, **60**, 4291–4305.

57 K. M. Noh, Y. B. Lee, W. H. Kwon, J. Y. Kang, W.-O. Choi and K. P. Chae, *Journal of Magnetics*, 2016, **21**, 308–314.

58 R. A. McCurrie, *Materials and Manufacturing Processes*, 1995, **10**, 1300–1301.

59 X. Lasheras, M. Insausti, J. M. de la Fuente, I. G. de Muro, I. Castellanos-Rubio, L. Marcano, M. L. Fernández-Gubieda, A. Serrano, R. Martin-Rodriguez, E. Garaio and others, *Dalton Transactions*, 2019, **48**, 11480–11491.

60 B. Aslibeiki, P. Kameli and H. Salamati, *J Appl Phys*, 2016, **119**, 63901.

61 A. A. de Almeida, F. Fabris, G. S. da Silva, K. R. Pirota, M. Knobel and D. Muraca, *ACS Appl Mater Interfaces*, 2025, **17**, 13083–13093.

62 O. K. Arriortua, M. Insausti, L. Lezama, I. G. de Muro, E. Garaio, J. M. de la Fuente, R. M. Fratila, M. P. Morales, R. Costa, M. Eceiza and others, *Colloids Surf B Biointerfaces*, 2018, **165**, 315–324.

63 E. A. Schultz-Sikma, H. M. Joshi, Q. Ma, K. W. MacRenaris, A. L. Eckermann, V. P. Dravid and T. J. Meade, *Chemistry of Materials*, 2011, **23**, 2657–2664.

64 H. Ma, L. Guo, H. Zhang, Y. Wang, Y. Miao, X. Liu, M. Peng, X. Deng, Y. Peng and H. Fan, *ACS Appl Bio Mater*, 2022, **5**, 3067–3074.

65 B. Aslibeiki, P. Kameli, M. H. Ehsani, H. Salamati, G. Muscas, E. Agostinelli, V. Foglietti, S. Casciardi and D. Peddis, *J Magn Magn Mater*, 2016, **399**, 236–244.

66 D. E. Zhang, X. J. Zhang, X. M. Ni, H. G. Zheng and D. D. Yang, *J Magn Magn Mater*, 2005, **292**, 79–82.

67 P. Guardia, B. Batlle-Brugal, A. G. Roca, O. Iglesias, M. D. P. Morales, C. J. Serna, A. Labarta and X. Batlle, *J Magn Magn Mater*, 2007, **316**, e756--e759.

68 E. C. Stoner and E. P. Wohlfarth, *Philosophical Transactions of the Royal Society of London. Series A, Mathematical and Physical Sciences*, 1948, **240**, 599–642.

69 D. Carta, M. F. Casula, A. Falqui, D. Loche, G. Mountjoy, C. Sangregorio and A. Corrias, *The Journal of Physical Chemistry C*, 2009, **113**, 8606–8615.

70 S. Yoon and K. M. Krishnan, *J Appl Phys*, 2011, **109**, 07B534.

71 M. Levy, A. Quarta, A. Espinosa, A. Figuerola, C. Wilhelm, M. García-Hernández, A. Genovese, A. Falqui, D. Alloyeau, R. Buonsanti, P. D. Cozzoli, M. A. García, F. Gazeau and T. Pellegrino, *Chemistry of Materials*, 2011, **23**, 4170–4180.

72 S. Kubickova, D. Niznansky, M. P. Morales Herrero, G. Salas and J. Vejpravova, *Appl Phys Lett*.

73 J. Carrey, B. Mehdaoui and M. Respaud, *J Appl Phys*, 2011, **109**, 83921.

74 T. E. Torres, E. Lima Jr, M. P. Calatayud, B. Sanz, A. Ibarra, R. Fernández-Pacheco, A. Mayoral, C. Marquina, M. R. Ibarra and G. F. Goya, *Sci Rep*, 2019, **9**, 3992.

75 D. Cabrera, A. Lak, T. Yoshida, M. E. Materia, D. Ortega, F. Ludwig, P. Guardia, A. Sathya, T. Pellegrino and F. J. Teran, *Nanoscale*, 2017, **9**, 5094–5101.

76 I. Castellanos-Rubio, I. Rodrigo, A. Olazagoitia-Garmendia, O. Arriortua, I. de Muro, J. S. Garitaonandia, J. R. n Bilbao, M. L. Fdez-Gubieda, F. Plazaola, I. aki Orue and others, *ACS Appl Mater Interfaces*, 2020, **12**, 27917–27929.

77 J.-P. Fortin, C. Wilhelm, J. Servais, C. Ménager, J.-C. Bacri and F. Gazeau, *J Am Chem Soc*, 2007, **129**, 2628–2635.

78 B. Mehdaoui, A. Meffre, J. Carrey, S. Lachaize, L.-M. Lacroix, M. Gougeon, B. Chaudret and M. Respaud, *Adv Funct Mater*, 2011, **21**, 4573–4581.

79 A. Lak, M. Cassani, B. T. Mai, N. Winckelmans, D. Cabrera, E. Sadrollahi, S. Marras, H. Remmer, S. Fiorito, L. Cremades-Jimeno and others, *Nano Lett*, 2018, **18**, 6856–6866.

80 D. Cabrera, A. Coene, J. Leliaert, E. J. Artés-Ibáñez, L. Dupré, N. D. Telling and F. J. Teran, *ACS Nano*, 2018, **12**, 2741–2752.

81 D. Cabrera, A. Lak, T. Yoshida, M. E. Materia, D. Ortega, F. Ludwig, P. Guardia, A. Sathya, T. Pellegrino and F. J. Teran, *Nanoscale*, 2017, **9**, 5094–5101.

82 R. Di Corato, A. Espinosa, L. Lartigue, M. Tharaud, S. Chat, T. Pellegrino, C. Ménager, F. Gazeau and C. Wilhelm, *Biomaterials*, 2014, **35**, 6400–6411.

83 P. T. Phong, L. H. Nguyen, L. T. H. Phong, P. H. Nam, D. H. Manh, I.--J. Lee and N. X. Phuc, *J Magn Magn Mater*, 2017, **428**, 36–42.

84 F. Soetaert, S. K. Kandala, A. Bakuzis and R. Ivkov, *Sci Rep*, 2017, **7**, 6661.

85 R. M. Fratila and J. M. De La Fuente, *Nanomaterials for magnetic and optical hyperthermia applications*, Elsevier, 2018.

86 G. Tommasini, S. Del Sol-Fernández, A. C. Flavián-Lázaro, A. Lewinska, M. Wnuk, C. Tortiglione and M. Moros, *Adv Funct Mater*, 2024, **34**, 2405282.

87 S. Del Sol-Fernández, Y. Portilla-Tundidor, L. Gutiérrez, O. F. Odio, E. Reguera, D. F. Barber and M. P. Morales, *ACS Appl Mater Interfaces*, 2019, **11**, 26648–26663.

88 D. Garcia-Soriano, P. Milán-Rois, N. Lafuente-Gómez, C. Navio, L. Gutiérrez, L. Cussó, M. Desco, D. Calle, Á. Somoza and G. Salas, *J Colloid Interface Sci*, 2022, **613**, 447–460.

View Article Online
DOI: 10.1039/D5NH00254K

The data supporting this article 'Unraveling the Mn^{2+} Substitution Effect on the Anisotropy Control and Magnetic Hyperthermia of $Mn_xFe_{3-x}O_4$ Nanoparticles' by the authors '*Oscar F. Odio, Giuseppina Tommasini, F. J. Teran, Jesus G. Ovejero, Javier Rubín, María Moros,* and *Susel Del Sol-Fernández*' have been included as part of Supplementary Information.